学　位　論　文

堀　　純　也

目　次

1. 主論文

Superconductivity and Phase Diagram of Tetragonal $La_{2-x}Sr_xCuO_4$ studied by Resistivity Measurements under Pressure
(圧力下の電気抵抗率測定による正方晶 $La_{2-x}Sr_xCuO_4$ の超伝導および相図の研究)
堀　純也

2. 公表論文

Correlation between superconductivity and in-plane resistivity in $La_{2-x}Sr_xCuO_4$
J. Hori, S. Iwata, H. Kurisaki, F. Nakamura, T. Suzuki, and T. Fujita
Journal of the Physical Society of Japan, **71**(2002)1346-1352.

3. 参考論文

(1) **Superconductor-insulator transition in under-doped cuprates**
T. Fujita, J. Hori, S. Iwata, Y. Yoshino, H. Kurisaki, T. Goko, Y. Yamane, and F. Nakamura
Physica C**364-365**(2001)274-277.

(2) **Effect of orthorhombic distortion on superconductivity in $La_{2-x}Sr_xCuO_4$**
T. Goko, F. Nakamura, J. Hori, and T. Fujita
Physica B**284-288**(2000)1053-1054.

(3) **Superconductivity in the tetragonal lattice of underdopd $La_{2-x}Sr_xCuO_4$**
T. Fujita, J. Hori, T. Goko, N. Kikugawa, and S. Iwata
Physica C**341-348**(2000)1939-1940.

(4) **Enhancement of conduction along the *c* axis in $La_{2-x}Sr_xCuO_{4-\delta}$ due to the impurity scattering**
N. Kikugawa, J. Hori, F. Nakamura, and T. Fujita
Journal of the Physical Society of Japan,**69**(2000)1177-1180.

(5) **Role of two-dimensional electronic state in superconductivity in $La_{2-x}Sr_xCuO_4$**
F. Nakamura, T. Goko, J. Hori, Y. Uno, N. Kikugawa, and T. Fujita
Physical Review B **61**(2000)107-110.

(6) **T_c enhancement in $La_{2-x}Sr_xCuO_4$ by anisotropic pressure**
T. Fujita, J. Hori, T. Goko, and F. Nakamura
International Journal of Modern Physics B **13**(1999)3655-3659.

(7) **T_c enhancement in $La_{2-x}Sr_xCuO_4$ under anisotropic pressure**
F. Nakamura, J. Hori, T. Goko, Y. Uno, N. Kikugawa, and T. Fujita
Journal of Low Temperature Physics, **117**(1999)1145-1149.

(8) **Impurity scattering effect on the anisotropic resistivity for $La_{2-x}Sr_xCuO_{4-\delta}$ with a wide range of x**
N. Kikugawa, J. Hori, F. Nakamura, and T. Fujita
Journal of Low Temperature Physics, **117**(1999)1139-1143.

(9) **Transport properties of $La_{2-x}Sr_xCuO_4$ under pressure**
F. Nakamura, T. Goko, J. Hori, Y. Uno, N. Kikugawa, and T. Fujita
Physica C**317-318**(1999)366-372.

主論文

Superconductivity and Phase Diagram of Tetragonal $La_{2-x}Sr_xCuO_4$ studied by Resistivity Measurements under Pressure

Jun'ya HORI

Department of Quantum Matter, ADSM,
Hiroshima University,
Higashi-Hiroshima 739-8530, Japan

March, 2002

Abstract

The correlation between the superconducting transition temperature (T_c) and two-dimensional metallic properties has been investigated in $La_{2-x}Sr_xCuO_4$(LSCO) by measuring in-plane resistivity (ρ_{ab}) over a wide rage of Sr concentration under anisotropic high pressure up to 8.0 GPa. Although the suppression of orthorhombic distortion by pressure is known to enhance T_c, the inter-layer compression brought about the weak localization in the electronic state of two-dimensional CuO_2 planes in the under-doped region. The collapse of two-dimensional electronic state probed by the metallic ρ_{ab} was the end of superconductivity in the under-doped cuprates. On the other hand, the overdoped cuprates lose superconductivity when the electronic structure changes from the two-dimensional metallic one to a strongly anisotropic but three-dimensional Fermi liquid system.

Furthermore, the phase diagram of T_c for tetragonal LSCO at "ambient" pressure has been investigated from the pressure dependence of T_c. The new phase diagram indicates that T_c draws so-called a bell-shape curve in the overdoped region. On the other hand, In the under-doped region, T_c shows linear dependence on carrier concentration x and a superconductor-insulator transition occurs discontinuously at a critical concentration $x_c \sim 0.05$.

Contents

1 Introduction

Since the discovery of high-T_c cuprates, a large number of experimental[1)] and theoretical[2)] investigations have been performed to characterize the electronic properties of the related cuprates constructing a generic phase diagram. The electronic phase diagram is an indispensable map for studying the implication of the peculiar normal-state characteristics in electron pairing at elevated temperatures. One of the most remarkable peculiarities is two dimensionality in the electronic state, which is believed to be responsible in part for high-T_c superconductivity. The two dimensionality arises from a stacked structure of conductive CuO_2 layers which the cuprates have in common.

Among a variety of superconducting cuprates, the lower-T_c materials, for example, $La_{2-x}Sr_xCuO_4$ (LSCO, $T_c \sim 38$ K), $Nd_{2-y}Ce_yCuO_4$ ($T_c \sim 25$ K) and $Bi_2Sr_2CuO_6$ ($T_c \sim 20$ K), have relatively simple structures. On the other hand, the higher-T_c cuprates, for example, $Bi_2Sr_2Ca_2Cu_3O_{10}$ ($T_c \sim 110$ K) and $YBa_2Cu_3O_7$ ($T_c \sim 90$ K), have rather complicated layers structures, This tendency indicates that fine tuning of the lattice is required to realize the two-dimensional electronic state in the CuO_2 planes favorable to the high-T_c superconductivity. The transition temperature (T_c) is sensitive also to disorder introduced by the chemical impurities[3)–5)] as well as by the structural distortion in the CuO_2 planes. Effects of high pressure[6)–8)] and epitaxial strain[9),10)] were reported for LSCO that the orthorhombic distortion, the tilting of CuO_6 octahedra or consequently the buckling of CuO_2 planes depresses T_c appreciably. The application of anisotropic pressure to LSCO[11)] was reported to enhance T_c up to ~ 52 K in the tetragonal phase that is the highest T_c reported so far in the La-214 systems. The T_c enhancement by expanding the inter-layer distance was also reported by epitaxial strain on LSCO thin films.[9),12)] $HgBa_2Ca_2Cu_3O_9$ having the highest T_c of 134 K (164 K under pressure[13)]) so far attained has flat CuO_2

planes again. Thus in addition to the carrier doping, the inter-layer spacing and the flatness of CuO_2 planes are the key parameters for higher-T_c superconductivity in cuprates.

As carriers are doped by chemical substitution or oxidation, the antiferromagnetism in a parent cuprate is suppressed and then the superconductivity appears in a restricted region above a critical carrier concentration as shown in the phase diagram of Fig.1. In the antiferromagnetic phase, both the in-plane resistivity (ρ_{ab}) and the out-of-plane resistivity (ρ_c) show a semiconductor-like upturn at low temperatures because slightly doped carriers are localized. With increasing carrier concentration, ρ_{ab} becomes to show metallic temperature dependence ($d\rho_{ab}/dT > 0$) and coincidently superconductivity appears. Even in the superconductive region above the critical concentration, the low-temperature upturn revives when the superconductivity is suppressed by the impurities[5] or by magnetic fields.[14)–16)] It suggests that the relation between the temperature dependence of ρ_{ab} and T_c provides a key for understanding the high-T_c superconductivity.

LSCO is one of the most suitable cuprates to investigate the relation between ρ_{ab} and T_c because of its simple crystal structure as shown in Fig.2 and of a wide range of controllable carrier concentration x from under-doped antiferromagnetic insulators to overdoped non-superconducting metals via superconductors. Hence, the T_c-x diagram of LSCO shown in Fig.1 is regarded as a generic phase diagram of high-T_c curates. However, LSCO undergoes a structural phase transition from a tetragonal phase to an orthorhombic phase as shown in Fig.1 and 3. The orthorhombic structure disturbs the superconductivity and obscures the intrinsic correlation between T_c and ρ_{ab} as reported earlier. In order to remove such difficulties, we have utilized the pressure, which stabilizes the tetragonal lattice and allows us to investigate the transport properties and T_c in the tetragonal phase. Moreover, we can widely control T_c by applying anisotropic pressure.[11)] In this work, we report the pressure

dependence of T_c and the temperature dependence of resistivity in the tetragonal phase of LSCO single crystals under pressure. The pressure dependence of T_c allows us to estimate the T_c^T, which is T_c in the tetragonal phase at ambient pressure, and to make a new phase diagram. The new phase diagram indicates that T_c^T depends linearly on carrier concentration x in the under-doped region. Furthermore, T_c^T vanishes discontinuously at a critical concentration $x_c \sim 0.05$, suggesting a first order transition. In the overdoped region, T_c^T follows a bell-shaped curve against x. In the vicinity of x_c in the under-doped region and of the overdoped boundary between superconductor and non-superconducting metal, the T_c-ρ_{ab} correlation is studied. Especially the upturn in the low-temperature ρ_{ab} is discussed in terms of weak localization.

2 Experimental

2.1 Single crystal growth of $La_{2-x}Sr_xCuO_4$

In order to study the correlation between two-dimensional transport properties and T_c of $La_{2-x}Sr_xCuO_4$(LSCO), we need high-quality single crystals. Single crystals of LSCO were grown by the traveling-solvent floating-zone (TSFZ) method using an infrared furnace (Nichiden, SC-M15HD) with two halogen lamps (USHIO INK.,100V-500W) as the heat source. The advantage of the TSFZ method is that large single crystals can be grown without contamination by impurities because no crucibles are needed. Figure 4 is an illustration of our crystal-growth process. The whole material is composed of three parts : a feed rod, a molten zone, and a as-grown single crystal. The feed rod is a polycrystal of LSCO. The molten zone, which lies on a common focus of the twin-elliptic mirrors, contains a cuprate with extra CuO as a solvent and the melting point is lower than that of the feed rod in order to localize the molten zone stably in the liquid phase. A typical composition of the solvent was shown in Table.1. Typical temperature reaches 1200 $\sim$ 1300 °C in the molten zone. The feed rod melts into the molten zone at a speed of $\sim$ 0.7 mm/hour with rotating clockwise at $\sim$ 35 rpm. A single crystal is grown at a typical speed of $\sim$ 1.0 mm/hour with rotating anticlockwise at $\sim$ 25 rpm. Single crystal growth is performed at the oxygen atmosphere of 0.3 MPa in the quartz tube in order to suppress the evaporation of CuO.

The most important point in obtaining high-quality single-crystals by the TSFZ method is to keep the the molten zone stable during the crystal growth. The condition of the molten zone is sensitive to cracks of the feed rod which are liable to absorb the solvent. Hence, we need a homogeneous and high-density feed rod to suppress extra absorption of the solvent into the feed rod. In order to make a homogeneous feed rod, we employed a sol-gel process. The stoichiometric amount of

dried powders of La_2O_3 (WAKO PURE CHEMICAL INDUSTRIES. LTD.), $SrCO_3$, and CuO (RARE METALLIC CO.,LTD.) were dissolved into nitric acid in a quarts flask. The purities of La_2O_3 and $SrCO_3$ are 99.99%, and that of CuO is 99.999%. The homogenized solution was dried at $\sim$ 400 °C for 24 hours, and then the nitrated powder was oxygenated at 900 °C in flowing O_2 atmosphere for 24 hours. The oxygenated powder was sintered three times in air at 950 °C, 1000 °C, and 1100 °C (1200 °C for overdoped region) . The sintered oxide was repeatedly pulverized between each heat treatment. After these heat treatments, no impurity was confirmed in oxygenated powder by X-ray diffraction as shown in Fig.5. Obtained powder was put into a rubber tube with 1 mol% CuO powder and formed into a rod shape by hydrostatic pressure of 0.14 GPa. After preliminary sintering at 920 °C for 10 hours, the rod was suspended in a furnace by Ni-Cr wire and sintered at 1180 $\sim$ 1200 °C for 15 hours. Typical dimensions of the feed rod were 5.5 mm in diameter and 70 mm in length.

The single crystal of LSCO with $x = 0.10$ grown by the TSFZ method and the Laue patterns are shown in Figs.6 and 7. Typical sizes of as-grown crystal were 4.0 mm in diameter and 40 mm in length.

2.2 Characterization of the single crystals

To characterize our single-crystallins samples, we measured the lattice parameters, the temperature dependence of magnetic susceptibility at ambient pressure, and Sr concentration. The lattice constants at room temperature are shown in Fig.8. With increasing x, the c axis monotonously expands below $x = 0.15$ where LSCO has the highest T_c of 38 K. The c-axis length slightly increases above $x = 0.15$ with increasing x. In the $x < 0.1$ region, the a axis and b axis in the orthorhombic notation are normalized by $\sqrt{2}$ in Fig.8. At room temperature, the tetragonal phase is stabilized above $x \sim 0.1$. The a axis decreases monotonously with increasing x. We

measured the magnetic susceptibility of the under-doped samples by using a SQUID magnetometer (Quantum Design INC.), because LSCO undergoes magnetic ordering in the under-doped region. In $x = 0.02$, antiferromagnetic order was observed below $T_N = 4.5$ K as shown in Fig.9. By tunneling experiments[17] on the same crystal, a structure, which may be connected with the pseudo gap, was observed at least up to $\sim$ 160 K although this crystal does not show superconductivity. Figures 10 and 11 show the magnetic susceptibilities of under-doped samples with a hysteresis between zero field cooling (ZFC) and field cooling (FC), which is so-called spin-glass behavior.[18),19)] Diamagnetic behavior was clearly observed in the ZFC curves of Fig.11 for $x = 0.045$ which is near the boundary concentration x_c . However, this is not bulk superconductivity as shown in Fig.12. The Sr-concentration x shown in Table.1 was determined within ± 0.005 for each crystal by electron probe microanalysis (EPMA). In the vicinity of the boundary between superconductor and insulator, slightly inhomogeneous part were observed in the as-grown single crystals. For the samples in the vicinity of $x \sim 0.05$, we chose a homogeneous part carefully and performed resistivity measurement under pressure. After resistivity measurements, we checked the Sr-concentration of the samples and confirmed that distribution of the Sr concentration in the samples was within ± 0.005. In this paper, we use the Sr concentration x determined after pressurization.

2.3 Resistivity measurement under pressure

For measurements of resistivity under pressure, crystals were cut into three types of samples as shown Fig.13: (i) a long stick of a parallelepiped along the [001] direction, so called the c axis, (ii) a long stick of a parallelepiped along the [110] direction in the tetragonal notation, (iii) a plate shape perpendicular to the c axis. The sample dimensions of each sample are listed in Table.2. Samples were annealed typically at 915°C for 50 hours and at 500°C for subsequent 50 hours in 0.1 MPa

flowing O_2 atmosphere. The electrodes were formed by gold paste (Tokuriki Chem., 8570) with heat treatment at 800°C for 15 minutes under flowing O_2 atmosphere. The samples with electrodes are illustrated in Fig.13.

A cubic anvil device was employed to generate pressure up to 8.0 GPa. A sample was put into a cylindrical Teflon cell (inside dimension is 1.5 mm in diameter and 1.7 mm in height) filled with an equal volume of mixture of Fluorinert FC70 and FC77 (3M Co. St. Paul, MN) as a pressure transmitting medium. The Teflon cell was mounted in the center of a 6 mm cubic pyrophyllite gasket. Figure 14 shows the schematic drawings of the gasket and the cubic anvil device. Our cubic anvil device is designed to produce an isotropic volume change of the sample space. The actual stress was expected to be anisitropic and stronger along the longer direction of the sample than that along the shorter direction in the presence of fairly large difference in compressibility and thermal expansion between the sample and the pressure-transmitting medium frozen at low temperatures and/or solidified at high pressures. The deviation from a hydrostatic pressure was roughly estimated[8] from the pressure dependence of T_c and the uniaxial-stress dependence of T_c that obtained from ultrasonic measurement.[20] For the under-doped samples, approximately 4% larger stress acts along the longer direction. In the case of the overdoped samples, the deviation attained approximately 20%. In this paper, we use the averaged value to express the pressure (P) following the previous work.[8] The resistivity was measured by a standard four-probes method from 4.2 to 300 K at each pressure which was kept constant within 3%. Temperature dependence of ρ_{ab} was measured before and after pressurization to confirm the reproducibility. Our experiment was performed in nondestructive condition in which the data were taken reproducibly. T_c's were determined by $\rho_{ab} = 0$.

3 Results

3.1 Resistivity at ambient pressure

The temperature dependence of ρ_{ab} and ρ_c at ambient pressure for (a) under-doped and (b) overdoped LSCO with various Sr concentrations in the vicinity of the boundary between superconducting and non-superconducting regions is shown in Fig.15 and Fig.16 respectively. In the under-doped region, ρ_c shows a semiconductor-like temperature dependence. On the other hand, the temperature dependence of ρ_{ab} changes with increasing x. In the slightly doped region($x < 0.05$), ρ_{ab} show a semiconductor-like upturn without superconductivity at low temperatures. The temperature dependence of ρ_{ab} for $x = 0.055$ and 0.06, near the boundary of low doping, still shows a semiconductor-like upturn at low temperatures. As x increases, T_c rises and ρ_{ab} becomes to show metallic temperature dependence ($d\rho_{ab}/dT > 0$ and $\rho_{ab} \propto T$) down to low temperatures in the normal state. In the overdoped region, both ρ_{ab} and ρ_c show a metallic temperature dependence in the normal state. Superconductivity disappears at a critical concentration around $x \sim 0.25$. For $x = 0.26$, ρ_{ab} and ρ_c deviate from T-linear dependence to $T^{1.5}$ variation.

3.2 Effect of the c-axis strain on ρ_{ab}

Figures 17(a), 18(a), 19(a), 20(a), and 21(a) show $\rho_{ab}(T)$ of LSCO with $x = 0.06$, 0.07, 0.08, 0.18, and 0.22, respectively, under several pressures up to 8.0 GPa. The shape of these samples is a long stick of the parallelepiped along the c axis and the stronger stress acted perpendicular to CuO_2 planes as schematically shown in the figures. The pressure dependence of T_c is shown for each sample in Figs.17(b), 18(b), 19(b), 20(b), and 21(b). The T_c-P curves changes the slope at a pressure P_d in each sample. The orthorhombic distortion vanishes at P_d and the tetragonal phase is stabilized above P_d. With increasing pressure, T_c in the tetragonal phase

reduces at a rate of $dT_c/dP = -3.0$ K/GPa for $x = 0.06$, -3.6 K/GPa for $x = 0.07$, -3.1 K/GPa for $x = 0.08$, -3.1 K/GPa for $x = 0.08$, -5.3 K/GPa for $x = 0.18$, and -3.0 K/GPa for $x = 0.22$. In the orthorhombic phase, T_c decreases at a rate of $dT_c/dP = -0.6$ K/GPa for $x = 0.07$ and -1.3 K/GPa for $x = 0.22$. On the contrary, T_c slightly increases at the rate of $dT_c/dP = +0.4$ K/GPa for $x = 0.06$ and $+0.6$ K/GPa for $x = 0.08$. For $x = 0.18$, we could not estimate the reduction rate of T_c in the orthorhombic phase because of a few data point. The difference in the pressure dependence of T_c is explained in terms of the competition mainly between the c-axis compression and the relaxation of orthorhombic distortion. In LSCO, the former contributes to lowering T_c,[11] whereas the latter contributes to enhancing T_c.[8),21)] When pressure in the range of $P < P_d$ is applied to the samples with $x = 0.06$ and 0.08, the increase of T_c due to the flattening of the CuO_2 planes slightly overcomes the decrease of T_c due to the c-axis compression. On the other hand, the T_c reduction due to the c-axis compression overcomes the T_c enhancement due to the relaxation of orthorhombic distortion for $x = 0.07$ and 0.22. The degree of the c-axis compression depends on the shape of the sample. The anisotropy in shape is larger in the sample with $x = 0.07$ than in the samples with $x = 0.06$ and 0.08 so that the compressive stress along the c axis acts more strongly on the sample with $x = 0.07$ than on the sample with $x = 0.06$ and 0.08. Although the shape of the $x = 0.22$ sample is almost the same as those for $x = 0.06$ and 0.08, the c-axis compression predominates because the T_c reduction due to the orthorhombic distortion is small by nature in the overdoped region.

In Figs.17(a), 18(a), 19(a), 20(a), and 21(a), the remarkable feature is that all samples show a semiconductor-like upturn of ρ_{ab} under pressure at low temperatures. With increasing pressure, T_c decreases in the tetragonal phase. The absolute value of ρ_{ab} at room temperature decreases by 22, 19, 30, 17, and 14% for $x = 0.06$, 0.07, 0.08, 0.18 and 0.22, respectively, when 8.0 GPa is reached. The low-temperature

upturn of ρ_{ab} is fairly large in the under-doped samples. The upturn was observed only above 5.0 GPa for $x = 0.18$ and above 6.5 GPa for $x = 0.22$.

3.3 Effects of in-plane stress on ρ_{ab}

Shown in Figs.22(a), 23(a), and 24(a) are the temperature dependence of ρ_{ab} for superconductive samples with $x = 0.07$, and 0.08 and an insulative sample with $x = 0.04$, respectively, under pressures up to 8.0 GPa. In these cases, the stronger stress acts in the [110] direction as shown in the insets of the figure by the schematic drawing of the sample. As pressure increases from ambient pressure, the absolute value of ρ_{ab} at room temperature decreases by 53, 36, and 28% for $x = 0.04$, 0.07, and 0.08 respectively, when 8.0 GPa is reached. The pressure dependence of T_c for $x = 0.07$ and 0.08 is shown in Fig.22(b) and 23(b). T_c increases at a rate of $dT_c/dP = +1.4$ K/GPa up to $P_d \sim 5$ GPa for $x = 0.07$ and at a rate of +2.3 K/GPa up to $P_d \sim 4$ GPa for $x = 0.08$. Above P_d, T_c decreases at a rate of $dT_c/dP = -0.7$ K/GPa for $x = 0.07$ and at a rate of -0.6 K/GPa for $x = 0.08$. In these measurements, T_c at 8.0 GPa are still higher than T_c at 0.1 MPa. The T_c enhancement for $P < P_d$ arises mainly from relaxing the orthorhombic distortion while the T_c reduction above P_d arises mainly from the c-axis compression. As shown in Fig.22(a) and 23(a), ρ_{ab} in the tetragonal phase ($P > P_d$) for $x = 0.07$ and 0.08 shows metallic temperature dependence ($d\rho_{ab}/dT > 0$) down to T_c. On the other hand, ρ_{ab} for $x = 0.04$ showed semiconductor-like temperature dependence up to 8.0 GPa. At low temperatures, a small hump of ρ_{ab} was observed in this sample at 1.5, 3.0, and 5.0 GPa as shown in Fig.24(b) but superconductivity did not appear up to 8.0 GPa even though the orthorhombic distortion was suppressed under pressure.

3.4 Effects of in-plane stress on ρ_c

Figures.25 and 27 show (a) temperature dependence of ρ_c under pressure and

(b) pressure dependence of ρ_c at 300 K up to 8.0 GPa. The shape of these samples is a thin plate perpendicular to the c axis and the stronger stress acted within CuO_2 planes as schematically shown in the figures. In these cases, strong in-plane stress expands the distance between CuO_2 planes with the help of Poison's ratio. As shown in Fig.25(b) and 27(b), ρ_c increased above $\sim$ 1.5 GPa with increasing pressure in consequence of inter-layer expansion. At ambient pressure, these samples show a semiconductor-like upturn at low temperatures. However, the drop of resistivity was observed with lowering temperature and increasing pressure as shown in Fig.26(a) and 28(a). A temperature T_c' determined by extrapolation to $\rho_c = 0$ for each sample is plotted in Fig.26(b) and 28(b). T_c' increases with relaxation of orthorhombic distortion below P_d and decreases with increasing pressure above P_d. The pressure dependence of T_c' is qualitatively same as the pressure dependence of T_c.

4 Discussion

4.1 Correlation between ρ_{ab} and T_c

To investigate the relation between T_c and ρ_{ab}, we discuss the experimental results mainly in the tetragonal phase, that is for $P > P_d$, where we do not need to take account of the buckling of CuO_2 planes. As shown in Fig.22 and 23, ρ_{ab} keeps metallic temperature dependence ($d\rho_{ab}/dT > 0$ in the normal state as far as T_c is relatively high. It indicates that the enhancement of ρ_{ab} at low temperatures is related to the decrease in T_c. The resistance $R_\square$ and conductance $G_\square$ per CuO_2 plane in the tetragonal phase under pressure are shown in (a) and (b) of Figs.29-31, for the samples near the boundary of superconducting and non-superconducting phase. Here we define the sheet resistance by $R_\square = \rho_{ab}/d$ and the sheet conductance by $G_\square = d/\rho_{ab} = 1/R_\square$, where $d = 6.6$ Å is the inter-layer distance at room temperature. As seen in Figs.29-31, the under-doped samples have critical values of $R_\square$ and $G_\square$ corresponding to the limit of $k_F l_{ab} \sim 1$, where k_F is the Fermi wave number and l_{ab} is the in-plane mean free path. The ordinary metal shows the localization for $k_F l < 1$, where the mean free path become shorter than the wave length of the electron at around the Fermi level. In a free electron model for two-dimensional materials, $k_F l_{ab}$ is given by $k_F l_{ab} = hd/\rho_{ab}e^2$, where h is the Plank constant and e is the electron charge. The limit $k_F l_{ab} = 1$ corresponds to $R_\square = h/e^2$ shown by dotted lines in (a) of Figs.29-31. If we assume the so-called preformed pair that is the charge pair formed in the normal state above T_c, the limitting value $R_\square = h/4e^2$ also shown in (a) of Figs.29-31 is known as a universal critical sheet resistance observed at the superconducting-insulating phase transition in the ultrathin-film systems.[22] In the overdoped sample shown in Fig.32(a) and 33(a), $R_\square$ is fairly small compared with those of under-doped samples. $R_\square$ or $G_\square$ above T_c has a $\ln T$ dependent region at low temperatures as shown in Figs.32 and 33 for

$x = 0.18$ and 0.22, respectively. This behavior is frequently observed in the case of Anderson's weak localization.[23),24)] The theoretical model of the weak localization in the two-dimensional systems suggests a logarithmic temperature dependence of resistivity $\rho \sim \ln(1/T)$ for boson systems[25)] and of conductance $G \sim \ln T$ for fermion systems.[26)] The corrective term of conductance due to the weak localization in the two-dimensional electrotonic system is given by $\Delta G = (\alpha e^2/2\pi^2\hbar) \ln T$ the prefactor of which is derived from a scaling law, where α is a constant parameter of the order $\alpha \sim 1$. The $\ln T$ dependence of $G_\square$ at low temperatures is well described as $G_\square = G_0 + \Delta G$, where G_0 is a constant value. Plots of T_c against α are given in Fig.34. In the under-doped region, superconducting-insulating phase transition occurs around $\alpha = 1 \sim 3$. We also checked the slope of $R_\square$ against $\ln T$ by fitting the data to $R_\square = R_0 - (Ah/4e^2) \ln T$, where R_0 is a constant value and A is a prefactor of $\ln T$ normalized by $h/4e^2$. Figure 35 shows T_c against A. The superconducting-insulating phase transition occurs around $A \sim 1$. Although we can not conclude whether these cases are regarded as a fermion system or a boson system only from the present data, these results support that the enhancement of ρ_{ab} in the under-doped samples is ascribable to the weak localization. And the metallic nature of CuO_2 planes at low temperatures is essentially important for high-T_c superconductivity.

In the overdoped sample with $k_F l_{ab} \gg 1$, the low temperature enhancement of ρ_{ab} were recognized only at 5.0, 6.5 and 8.0 GPa for $x = 0.18$ and 6.5 and 8.0 GPa for $x = 0.22$. The temperature range where $R_\square$ and $G_\square$ show the $\ln T$ dependence is quite narrow compared with under-doped samples. As seen in Figs.34 and 35, α and A for the overdoped sample deviate far from those for under-doped samples. Thus for $x = 0.22$, it is difficult to ascribe the low-temperature upturn of ρ_{ab} to the weak localization. In the overdoped region, ρ_{ab} is well fitted by $\rho_{ab} = \rho_0 + \beta T^n$, except for the low-temperature ρ_{ab} at 6.5, 5.0 and 8.0 GPa for $x = 0.18$ and at 6.5 and 8.0 GPa for $x = 0.22$. The fitted lines for 3.0, 5.0 and 8.0 GPa for $x = 0.18$

and 2.0, 5.0 and 8.0 GPa for $x = 0.22$ are representatively shown in Fig.36 by the broken lines. T_c are also plotted against fitting parameters ρ_0, β, and n in Fig.37, 38, and 39, respectively. With increasing pressure, ρ_0 and n increase while T_c decreases monotonously against ρ_0 and n. In the case of chemical doping with Zn,[5] for example, T_c-variation is usually correlated with ρ_0 due to the impurities. The similar correlation between ρ_0 and T_c is seen in Fig.37. However the present data reveals that the change in T_c is described as a function of β and n. As n approaches 1.5, T_c tends to vanish as demonstrated in Fig.39. The value $n \sim 1.5$ is also observed for $x = 0.26$ at ambient pressure. β for $x = 0.22$ appears to approach the value for $x = 0.26$ with decreasing T_c. The non-superconducting LSCO with $x = 0.26$ has the tetragonal structure at ambient pressure. The increase of n indicates that the Fermi liquid state is formed as the ground state instead of superconductivity.

When carriers are introduced by substituting Sr for La in LSCO, Sr distributes randomly in the insulative block layer between the CuO_2 planes. The carriers are strongly confined in the CuO_2 planes[27] in an under-doped region. If the inter-layer distance is reduced in the under-doped region by applying anisotropic pressure, the random distribution of Sr in the block layer will increase the disordered potential in the CuO_2 planes, which brings about the weak localization of carriers. With further doping Sr, the effect of randomness may be reduced because the carrier number increases and consequently the overlap of the carrier wave function increases. In the overdoped region, the c-axis compression leads the sample to approach tree dimensional metal. We suspect that the low-temperature upturn of ρ_{ab} observed in the samples with $x = 0.18$ at 5.0, 6.5 and 8.0 GPa and with $x = 0.22$ at 6.5 and 8.0 GPa are not intrinsic nature in the overdoped region. The ρ_{ab} could be contaminated by the upturn of ρ_c under pressure in the overdoped region, because the carriers can be easily transferred across the block layer. Although ρ_c also shows metallic temperature dependence in the overdoped LSCO at ambient pressure, the

low temperature upturn of ρ_c at high pressures is reported by Goko *et.al.*[28] In addition, we can not overlook the effect of the apical oxygen, which will give rise to stronger perturbation on the electronic state of confined carriers in the CuO_2 planes with increasing pressure.

4.2 Phase diagram for superconductivity in the tetragonal phase

By extrapolating T_c in the high-pressure tetragonal phase to the ambient pressure, we can estimate T_c^T, which is T_c in the tetragonal phase at ambient pressure, as reported by Goko *et.al.*.[8] T_c^T is indicated for each sample in the plot of T_c against pressure. The T_c^T-x diagram plotted in Fig.40 is regarded as a phase diagram for the tetragonal LSCO. The data estimated from the polycrystals[6] and single crystals[28),29)] in the optimal and overdoped region are also plotted in Fig.40. In overdoped region, where the suppression of T_c due to the orthorhombic distortion is small, T_c^T follows a well-known bell-shape curve. On the other hand, T_c^T in under-doped region varies rather linearly with increasing carrier concentration x above $x \sim 0.05$. The similar tendency for various cuprates was observed in the plot of T_c against the muon-spin-relaxation rate,[30] which is proportional to the superconducting carrier density, though T_c is not only in the tetragonal one.

T_c^T's estimated from the drop of ρ_c shown for $x = 0.035$ and 0.045 in Fig.26 and 28 are plotted as open circles in Fig.40. Recently, the existence of the intrinsic phase separation or inhomogeneity has been reported by the scanning SQUID microscopy of LSCO thin films[31] and by the low-temperature scanning tunnelling microscopy/spectroscopy(STM/S) of Bi-2212.[32] The drop of resistivity under high pressure is also explained by the inhomogeneity. At ambient pressure, the superconductivity suppressed by the orthorhombicity. In the case of the stick shape sample along [110] shown in Fig.24, the superconducting trace appears as the hump of

the ρ_{ab} by suppressing the orthorhombic structure. However, the insulator phase overcomes the superconductivity in this case. On the other hand, the plate shape samples shown in Fig.26 and 28 are more favorable to superconductivity. With the help of the tetragonal structure and the enhancement of two dimensionality due to the expansion of the c axis, the samples were near displaying superconductivity. However, resistivity did not become zero because the superconducting fraction was so small. Both insulating phase and superconducting phase may coexist in the boundary region just like a first-order transition. We checked Sr concentration in these samples in detail by EPMA. The Sr concentration was $x \pm 0.005$ for each sample. ThE variation is within experimental error. If there is any inhomogeneity of Sr concentration, the distribution width of Sr is less than $\sim 2\mu$m, which is the spot size of the electron beam. The discontinuous change has been reported also in the incommensurate spin correlation observed in the vicinity of (π, π) of the reciprocal space by neutron scattering.[33] The incommensurate spin modulation changes suddenly from a vertical (or parallel) to diagonal one with decreasing hole concentration across $x \sim 0.05$, although the experiments has been performed on single-crystals of LSCO with orthorhombic structure. In addition, homogeneous single crystals in the vicinity of $x_c \sim 0.05$ are quite hard to be grown. We suspect that the difficulty in crystal growth is due to the intrinsic inhomogeneity accompanied by the first order transition. If the antiferromagnetic phase is confirmed to exist for $x \leq 0.05$ in the tetragonal lattice, the phase diagram of LSCO is similar to electron-doped $Nd_{2-y}Ce_yCuO_4$, and the electron-hole symmetry will be fully established in the cuprates.

5 Conclusions

The resistivity of LSCO has been studied in the vicinity of the boundary between superconducting and non-superconducting phases under anisotropic pressure to clarify the correlations between T_c and ρ_{ab} in the tetragonal phase, and to reveal the phase diagram for superconductivity in the tetragonal phase at ambient pressure.

In the under-doped region, T_c^T depends linearly on Sr concentration x and shows discontinuous change at a critical concentration $x_c \sim 0.05$. The bulk superconductivity do not appear in the $x < 0.05$ region even in the tetragonal phase. In the vicinity of x_c, ρ_{ab} shows a semiconductor-like upturn at low temperatures as T_c is depressed by pressure. The upturn of ρ_{ab} exhibits logarithmic temperature dependence of the conductance and resistance per CuO_2 plane even in the tetragonal phase. The $\ln T$-variation of the conductance and resistance suggests the weak localization of the in-plane electronic state. The weak localization arises from the random potential introduced by Sr-distribution in the insulative block layers or from the perturbation by the apical oxygen which disturbs the two-dimensional electronic state in the CuO_2 planes. The localization of two-dimensional electronic state essentially governs the superconductor-insulator transition in the under-doped region.

In the overdoped region, T_c^T's follows a bell-shape curve. In this region, the upturn of ρ_{ab} observed at high pressures is small compared with that for under-doped samples, and the temperature dependence remains metallic down to low temperatures. T_c appears to correlate well with n in the scalling $\rho_{ab} = \rho_0 + \beta T^n$. The superconductivity in the overdoped region disappears corresponding to the change in electronic structure from two-dimensional metallic state confined in the CuO_2 planes to the anisotropic but three-dimensional Fermi liquid.

Two-dimensional metallic conduction of the CuO_2 planes probed by ρ_{ab} is proposed to be an essential criterion for the appearance of superconductivity in the cuprates.

Acknowledgments

The author is grateful to Professor Toshizo Fujita for giving him valuable advice, stimulating discussion and continuous encouragement trough the course of this work. He also wishes to express his sincere thanks to Associate Professor Takashi Suzuki, Doctor Fumihiko Nakamura, and Doctor Masakazu Ito for numerous discussion and useful advice. He is grateful to Doctor Naoki Kikugawa and Shigenobu Sakita for technical advices of single crystal growth of LSCO, to Doctor Tatsuo Goko for technical advices and support of high-pressure experiment with cubic anvil device, to Shingo Iwata, Hiromi Kurisaki, Michio Koga, and Futoshi Nagasaki for technical support, and to other Fujita Lab. members for generous collaboration. He would like to express his appreciation to Professor Toshikazu Ekino for the discussion on tunneling characteristics and Doctor Yasuhiro Shibata, the Instrument Center for Chemical Analysis, Hiroshima University for EPMA. His thanks are also due to the Cryogenic Center of Hiroshima University for supplying the sufficient amount of liquid helium. This work is supported by a Grant-in-Aid for Scientific Research from the Ministry of Education, Culture, Sports, Science and Technology of Japan.

References

1) See, for example, T. Fujita, Y. Aoki, Y. Maeno, J. Sakurai, H. Fukuba, H. Fujii, T. Okamoto, K. Kumagai, M. Kurisu, H. Kadomatsu, and H. Fujiwara, Jpn. J. Appl. Phys. **26** (1987) 1041. for LBCO and LSCO, J. B. Torrance, Y. Tokura, A. I. Nazzal, A. Bezinge, T. C. Huang, and S. S. P. Parkin, Phys. Rev. Lett. **61**(1988)1127. for LSCO, H. Takagi, S. Uchida, and Y. Tokura, Phys. Rev. Lett. **62**(1989)1197. for NCCO, and R. J. Cava, A. W. Hewat, E. A. Hewat, B. Batlogg, M. Maresio, K. M. Rabe, J. J. Krajewski, W. F. Peck Jr, and L. W. Rupp Jr, Physica C **165**(1990)419. for YBCO.

2) See, for example, P. A. Lee, and N. Nagaosa, Phys. Rev. B **46** (1992) 5621, T. Tanamoto, H. Kohno, and H. Fukuyama, J. Phys. Soc. Jpn. **63**(1994)2739. and V. J. Emery and S. A. Kivelson, Nature **374**(1995)434. based on RVB model, S. C. Zhang, Science **275**(1997)1089. based on SO(5) theory.

3) Y. Maeno, T. Tomita, M. Kyogoku, S. Awaji, Y. Aoki, K. Hoshino, A. Minami, and T. Fujita, Nature **328** (1987) 512.

4) T. Siegrist, L. F. Schneemeyer, J. V. Waszczak, N. P. Singh, R. L. Opila, B. Batlogg, L. W. Rupp, and D. W. Murphy, Phys. Rev. B **36** (1987) 8365.

5) Y. Fukuzumi, K. Mizuhashi, K. Takenaka, and S. Uchida, Phys. Rev. Lett. **76** (1996) 684.

6) N. Yamada and M. Ido, Physica C **203** (1992) 240.

7) H. Takahashi, H. Shaked, B. A. Hunter, P. G. Radaelli, R. L. Hitterman, D. G. Hinks, and J. D. Jorgensen, Phys. Rev. B **50** (1994) 3221.

8) T. Goko, F. Nakamura, and T. Fujita, J. Phys. Soc. Jpn. **68** (1999) 3074.

9) J. P. Locquet, J. Perret, J. Fompeyrine, E. M achler, J. W. Seo, and G. V. Tendeloo, Nature **394** (1998) 453.

10) J. S. Zhou, J. B. Goodenough, H. Sato, and M. Naito, Phys. Rev. B **59** (1999) 3827.

11) F. Nakamura, T. Goko, J. Hori, Y. Uno, N. Kikugawa, and T. Fujita, Phys. Rev. B **61** (2000) 107.

12) H. Sato, A. Tsukada, M. Naito, and A. Matsuda, Phys. Rev. B **61** (2000) 12447.

13) L. Gao, Y. Y. Xue, F. Chen, Q. Xiong, R. L. Meng, D. Ramirez, C. W. Chou, J. H. Eggert, and H. K. Mao, Phys. Rev. B **50** (1994) 4260.

14) Y. Ando, G. S. Boebinger, A. Passner, T. Kimura, and K. Kishio, Phys. Rev. Lett. **75** (1995) 4662.

15) G. S. Boebinger, Y. Ando, A. Passner, T. Kimura, M. Okuya, J. Shimoyama, K. Kishio, K. Tamasaku, N. Ichikawa, and S. Uchida, Phys. Rev. Lett. **77** (1996) 5417.

16) P. Wagner, K. Q. Ruan, I. Gordon, J. Vanacken, V. V. Moshchalkov, and Y. Bruynseraede, Physica C **356** (2001) 107.

17) T. Ekino, S. Hashimoto, H. Fujii, J. Hori, F. Nakamura, and T. Fujita, Physica C **357-360** (2001) 158.

18) F. C. Chou, N. R. Belk, M. A. Kastner, and R. J. Birgeneau, Phys. Rev. Lett. **75** (1995) 2204.

19) S. Wakimoto, S. Ueki, and Y. Endoh, Phys. Rev. B **62** (2000) 3547.

20) M. Nohara, T. Suzuki, Y. Maeno, T. Fujita, I. Tanaka, and H. Kojima, Phys. Rev. B **52** (1995) 570.

21) F. Gugenberger, C. Meingast, G. Roth, K. Grube, V. Breit, T. Weber, H. Wühl, S. Uchida, and Y. Nakamura, Phys. Rev. B **49** (1994) 13137.

22) T. Pang, Phys. Rev. Lett. **62** (1989) 2176.

23) G. J. Dolan and D. D. Osheroff, Phys. Rev. Lett. **43** (1979) 721.

24) S. Kobayashi, F. Komori, Y. Ootuka, and W. Sasaki, J. Phys. Soc. Jpn. **49** (1980) 1635.

25) D. Das and S. Doniach, Phys. Rev. B **57** (1998) 14440.

26) E. Abrahams, P. W. Anderson, D. C. Licciardello, and T. V. Ramakrishnan, Phys. Rev. Lett. **42** (1979) 673.

27) N. Kikugawa, J. Hori, F. Nakamura, and T. Fujita, J. Phys. Soc. Jpn. **69** (2000) 1177.

28) T. Goko, F. Nakamura, N. Kikugawa, Y. Uno, S. Sakita, and T. Fujita, Physica C **282-287** (1998) 1151.

29) F. Nakamura, T. Goko, N. Kikugawa, J. Hori, Y. Uno, and T. Fujita, Physica C **317-372** (1999) 366.

30) Y. J. Uemura, G. M. Luke, B. J. Sternlieb, J. H. Brewer, J. F. Carolan, W. N. Hardy, R. Kadono, J. R. Kempton, R. F. Kiefl, S. R. Kreitsman, P. Mulhern, T. M. Riseman, D. L. Williams, B. X. Yang, S. Uchida, H. Takagi, J. Gopalakrishnan, A. W. Sleight, M. A. Subramanian, C. L. Chien, M. Z. Cieplak, G. Xiao, V. Y. Lee, B. W. Statt, C. E. Stonach, W. J. Kossler, and X. H. Yu, Phys. Rev. Lett. **62** (1989) 2317.

31) I. Iguchi, T. Yamaguchi, and A. Sugimoto, Nature **412** (2001) 420.

32) S. H. Pan, J. P. Neal, R. L. Badzey, C. Chamom, H. Ding, J. R. Engelbrecht, Z. Wang, H. Eisaki, S. Uchida, A. K. Gupta, K.-W. Ng, E. W. Hudson, K. M. Lang, and J. C. Davis, Nature **413** (2001) 282.

33) S. Wakimoto, G. Shirane, Y. Endoh, K. Hirota, S. Ueki, K. Yamada, R. J. Birgeneau, M. A. Kastner, Y. S. Lee, P. M. Gehring, and S. H. Lee, Phys. Rev. B **60** (1999) 769.

Table 1: Typical composition of a feed rod and a solvent. Sr concentration x of the grown single crystals determined by EPMA is also shown.

Feed rod	Solvent [mol%]			Grown crystal
x (nominal)	La_2O_3	$SrCO_3$	CuO	x (EPMA)
0	15.00	0	85.00	0
0.02	19.60	0.40	80.00	0.02
0.04	19.22	0.78	80.00	0.035~0.040
0.05	19.02	0.98	80.00	0.045~0.05
0.06	14.13	0.87	85.00	0.05~0.06
0.07	18.65	1.35	80.00	0.063~0.070
0.08	18.46	1.54	80.00	0.078~0.08
0.10	18.10	1.90	80.00	0.1
0.18	21.21	11.44	67.35	0.18
0.25	21.21	13.85	64.94	0.22
0.32	21.21	16.28	62.51	0.26

Table 2: Dimensions of the samples for resistivity measurements. A schematic drawing of the samples is shown in Fig.13

x	Shape	Measurement	Size (mm^3)
0.02	plate (Fig.13(iii))	ρ_c	0.45 × 0.45 × 0.06
0.035	plate (Fig.13(iii))	ρ_c	0.45 × 0.45 × 0.06
0.04	stick (Fig.13(ii))	ρ_{ab}	0.73 × 0.25 × 0.20
0.045	plate (Fig.13(iii))	ρ_c	0.45 × 0.45 × 0.06
0.06	stick (Fig.13(i))	ρ_{ab}	0.80 × 0.30 × 0.25
0.07	stick (Fig.13(i))	ρ_{ab}	0.80 × 0.28 × 0.20
0.07	stick (Fig.13(ii))	ρ_{ab}	0.73 × 0.25 × 0.20
0.08	stick (Fig.13(i))	ρ_{ab}	0.80 × 0.30 × 0.25
0.08	stick (Fig.13(ii))	ρ_{ab}	0.73 × 0.25 × 0.20
0.18	stick (Fig.13(i))	ρ_{ab}	0.78 × 0.30 × 0.25
0.22	stick (Fig.13(i))	ρ_{ab}	0.78 × 0.30 × 0.25

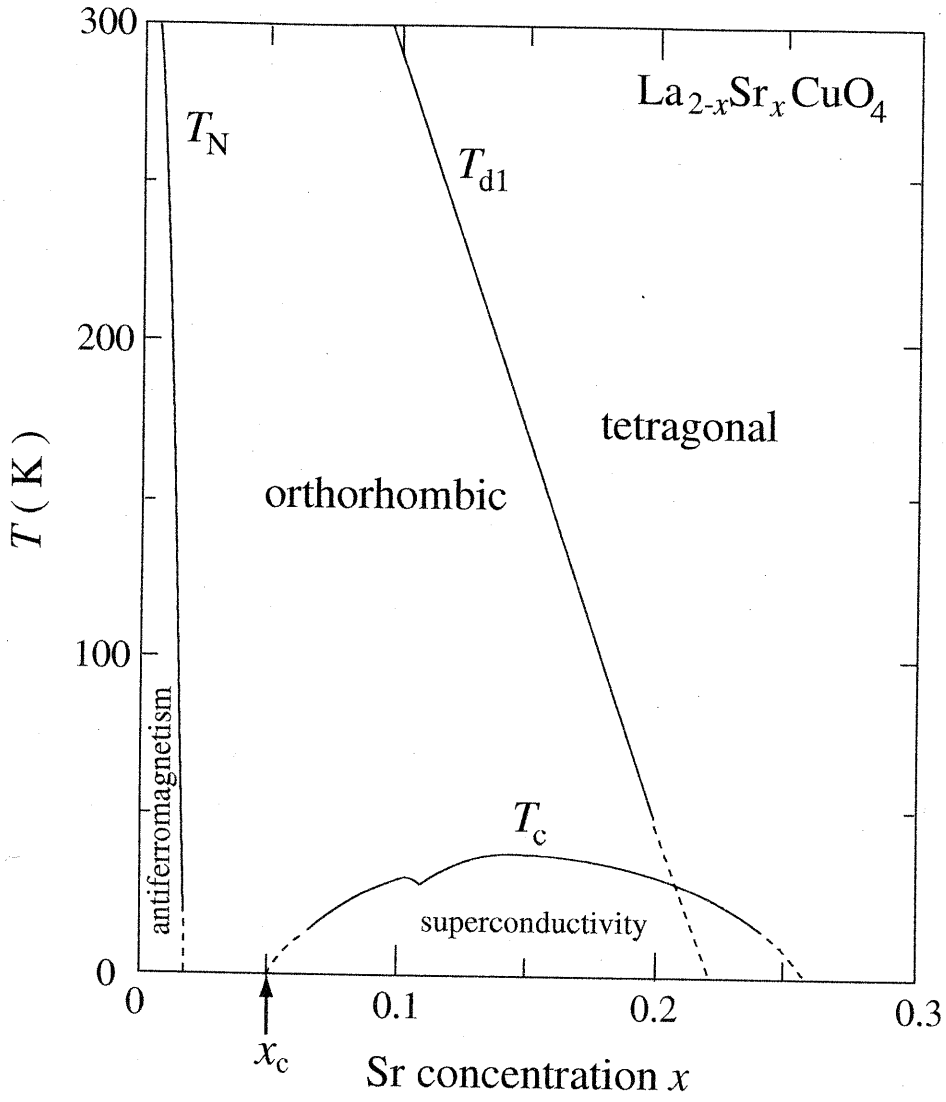

Figure 1: Phase diagram of $La_{2-x}Sr_xCuO_4$. As carriers are doped by substituting Sr for La, antiferromagnetism in a parent cuprate La_2CuO_4 is rapidly suppressed and superconductivity appears in a restricted region above a critical carrier concentration $x_c \sim 0.05$. LSCO undergoes a structural phase transition from tetragonal phase to orthorhombic phase at T_{d1}.

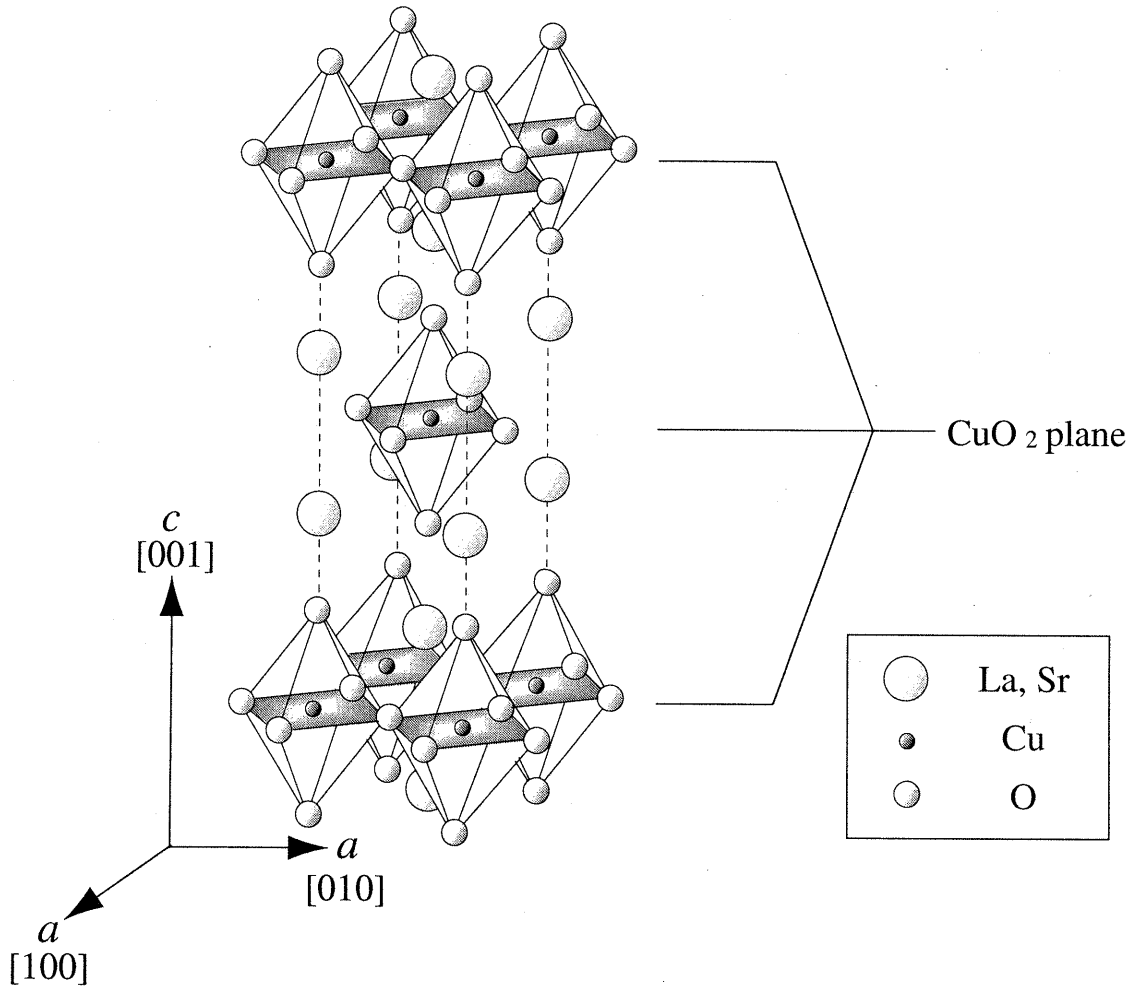

Figure 2: Crystal structure of $La_{2-x}Sr_xCuO_4$ in the tetragonal phase. LSCO has a stacked structure of conductive CuO_2 layers sandwiched by insulative $(La, Sr)_2O_2$ layers , which gives rise to two dimensionality in the electronic state.

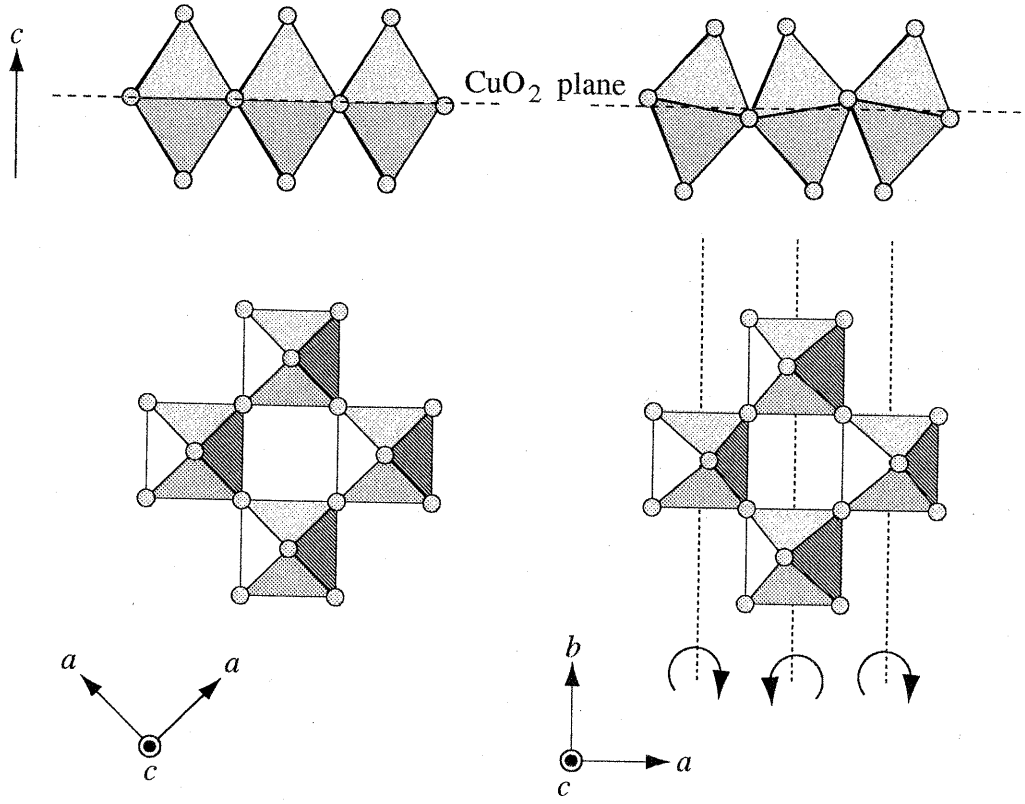

Figure 3: Schematic diagrams of CuO_6 octahedra in the tetragonal structure and orthorhombic structure. LSCO undergoes the structural phase transition from a tetragonal phase to an orthorhombic phase at T_{d1} (see Fig.1). The orthorhombic phase is due to the tilting of CuO_6 octahedra or consequently the buckling of CuO_2 planes.

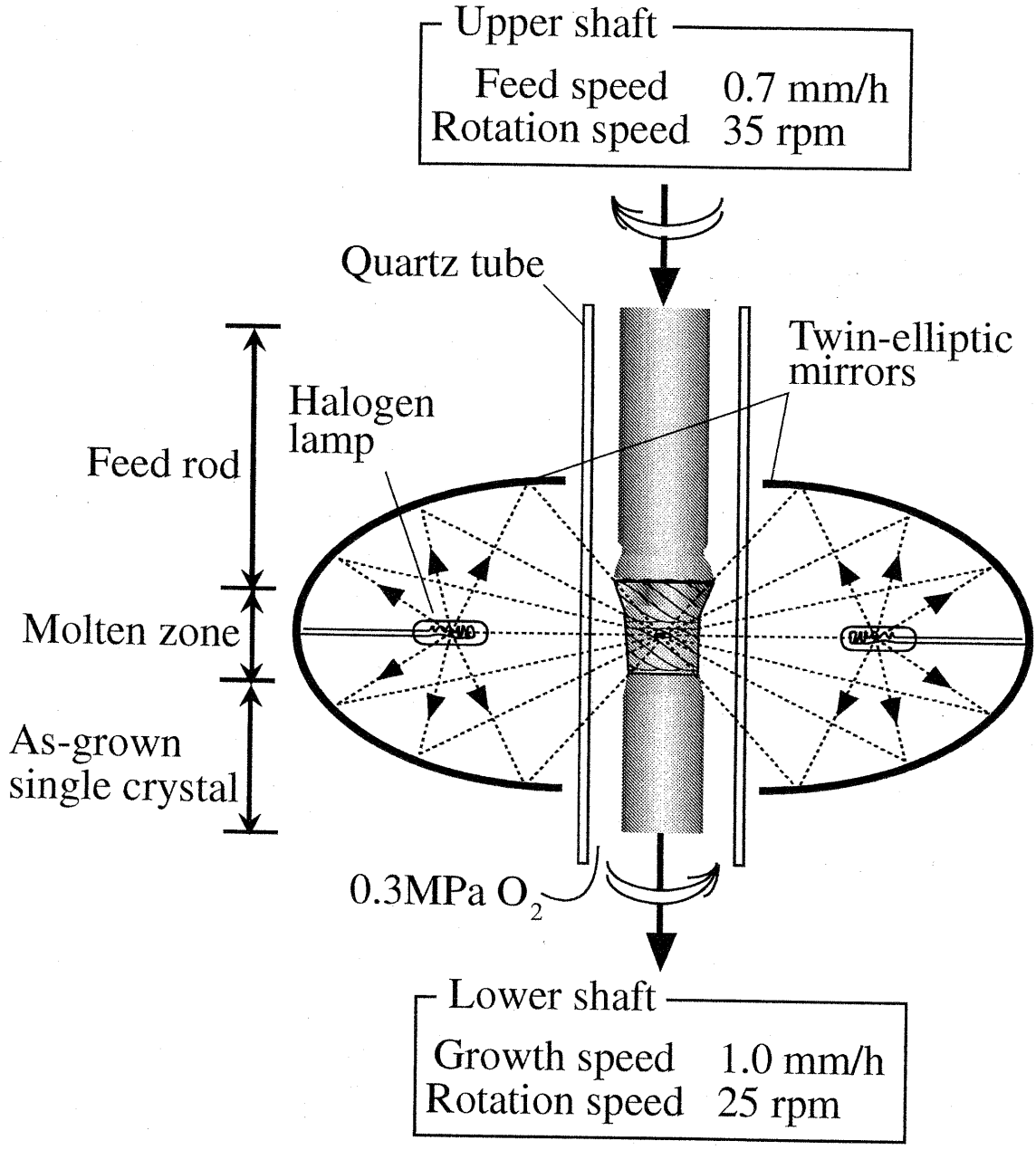

Figure 4: Illustration of traveling solvent floating zone (TSFZ) method. A single crystal is grown at the oxygen atmosphere of 0.3 MPa in the quartz tube in order to suppress the evaporation of CuO. The feed rod melts into the molten zone at a speed of $\sim$ 0.7 mm/hour. The molten zone lies on a common focus of the twin-elliptic mirrors. A single crystal is grown at a typical speed of $\sim$ 1.0 mm/hour.

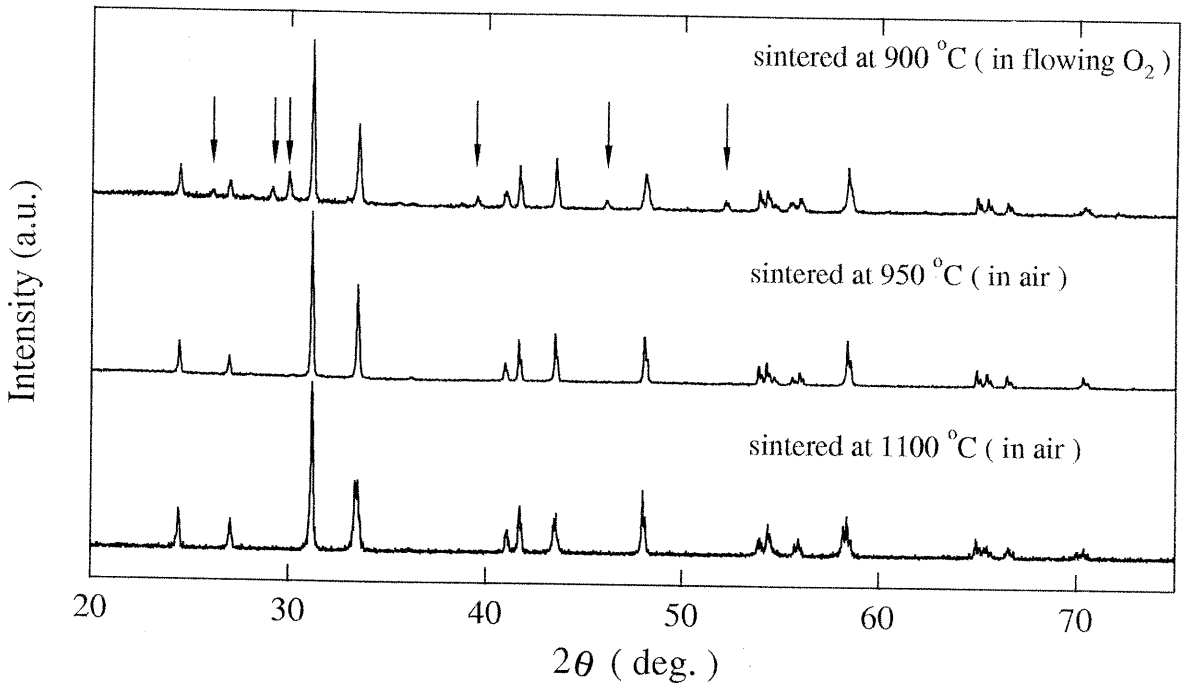

Figure 5: X-ray diffraction pattern of $La_{2-x}Sr_xCuO_4(x = 0.10)$ powder used to form a feed rod. Arrows indicate peaks due to the impurities, for example, La_2O_3, $La(OH)_3$, and $La_{3-x}Sr_xCu_2O_6$. After heat treatment above 950°C, no impurity peak was observed.

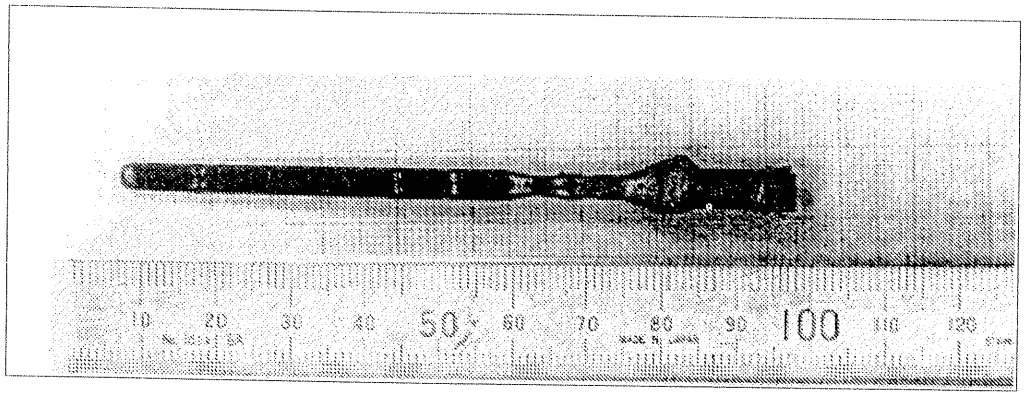

Figure 6: As-grown single crystal of $La_{2-x}Sr_xCuO_4(x = 0.10)$ grown by the TSFZ method. Typical sizes of as-grown crystal were 4.0 mm in diameter and 40 mm in length.

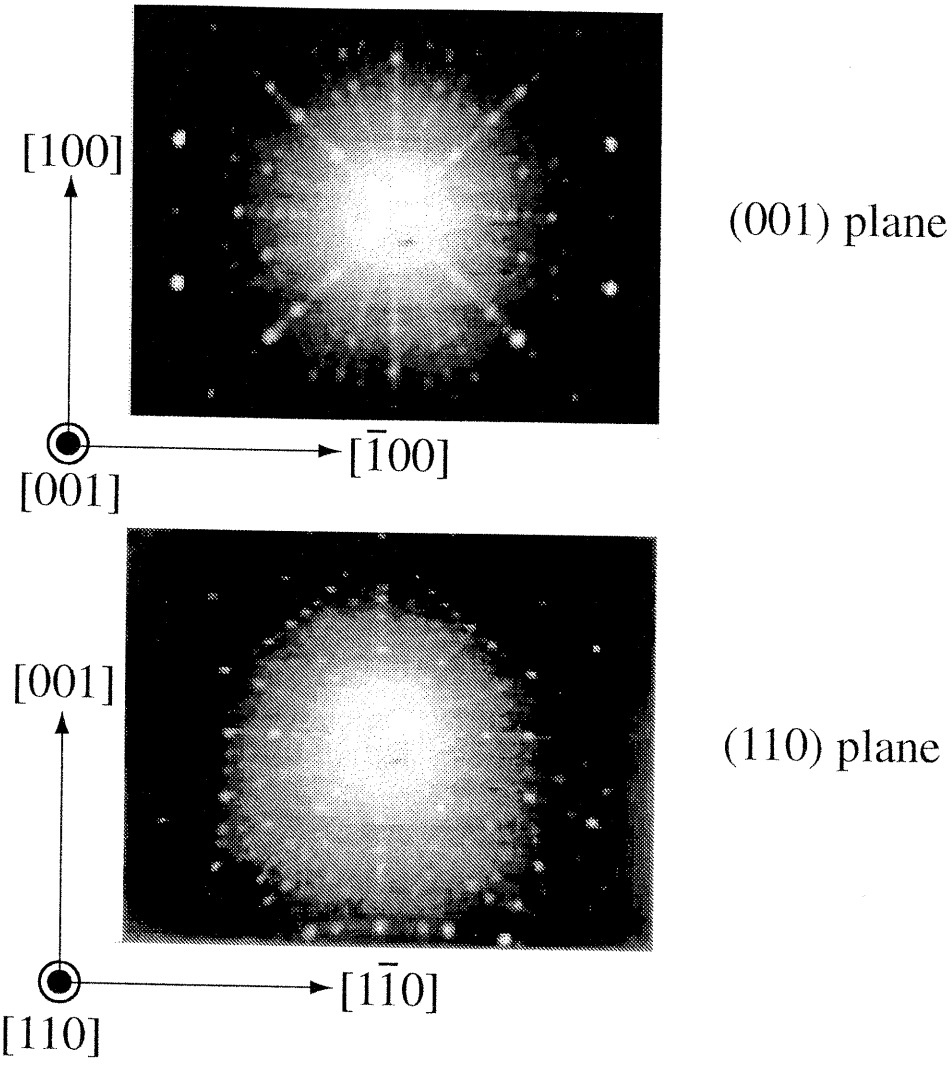

Figure 7: Laue spots of an LSCO single crystal for the (001) and the (110) planes in the tetragonal notation.

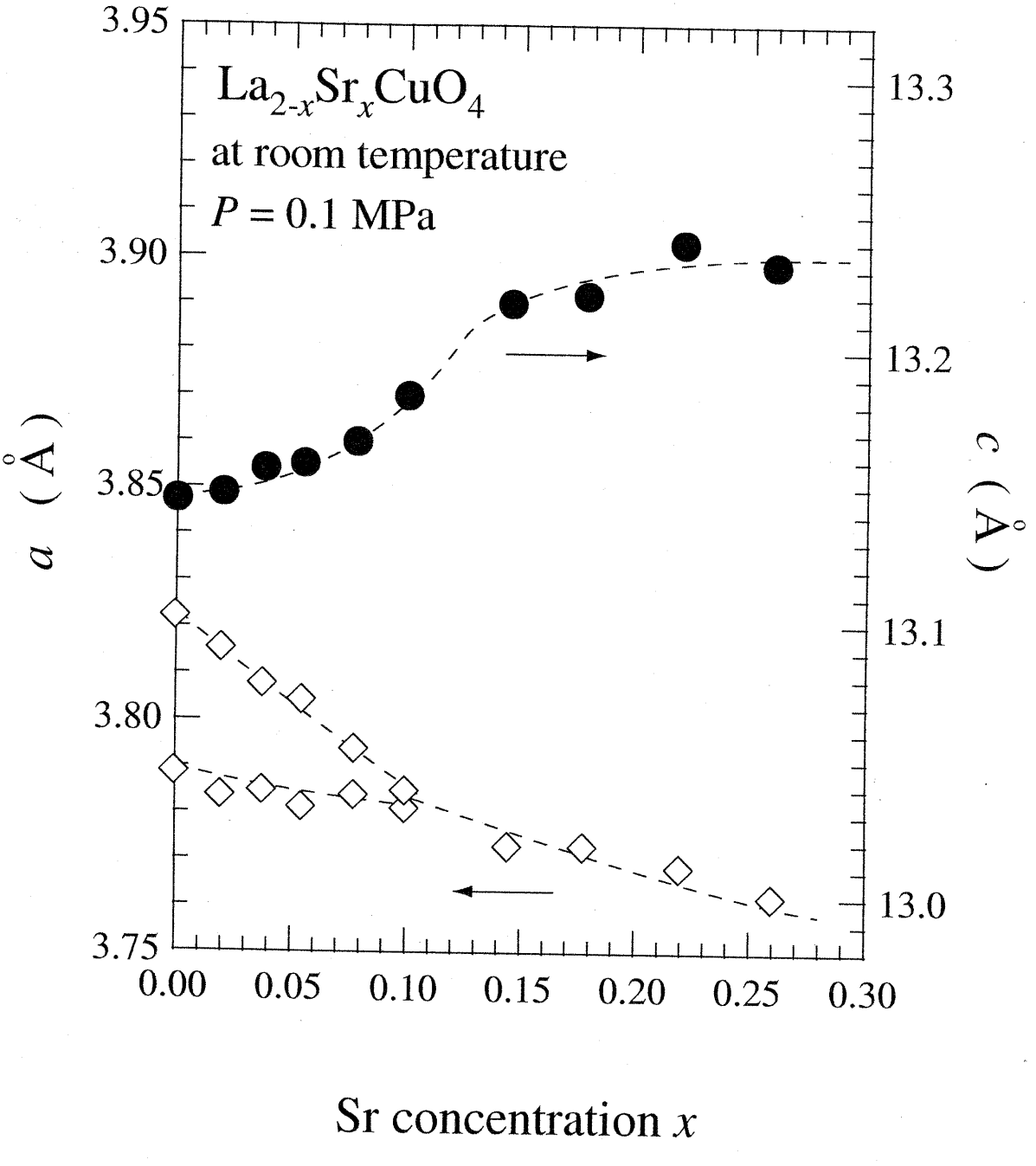

Figure 8: Lattice parameters of LSCO with various Sr concentrations x at room temperature. The a and c axes are determined by X-ray diffraction measurements at 0.1 MPa. The a axis and b axis in the orthorhombic notation normalized by $\sqrt{2}$ is shown in the figure as the a axis below $x = 0.1$.

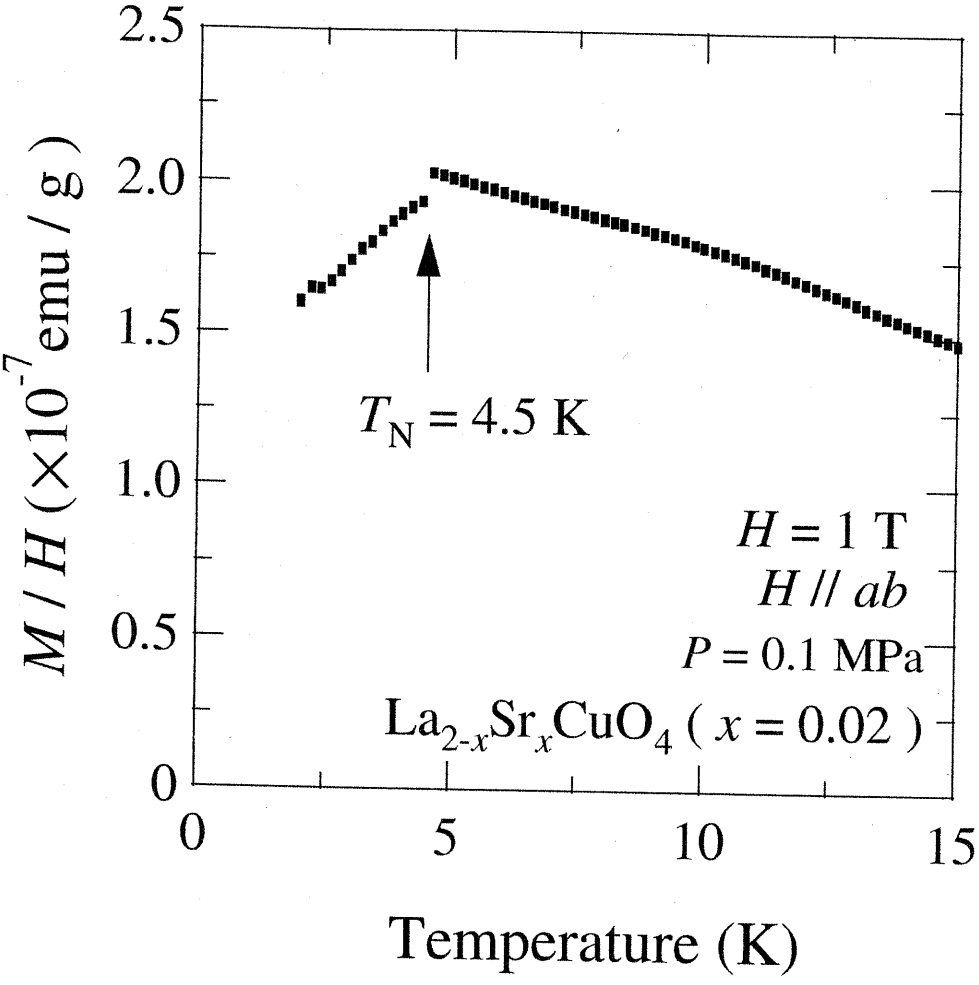

Figure 9: Temperature dependence of magnetic susceptibility at 1 T for $x = 0.02$. Antiferromagnetic transition was observed at 4.5 K.

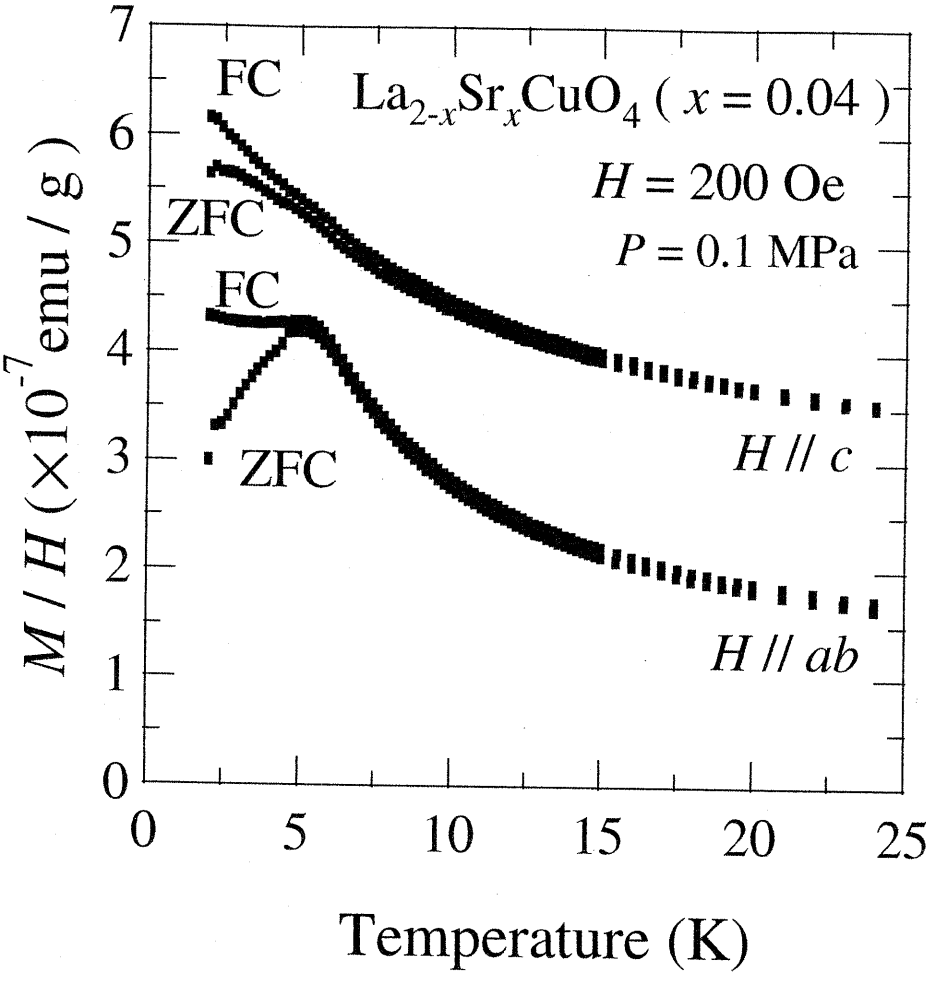

Figure 10: Temperature dependence of magnetic susceptibility at $H = 200$ Oe for $x = 0.04$. A hysteresis of M/H between zero field cool(ZFC) and field cool(FC) was observed below 5 K.

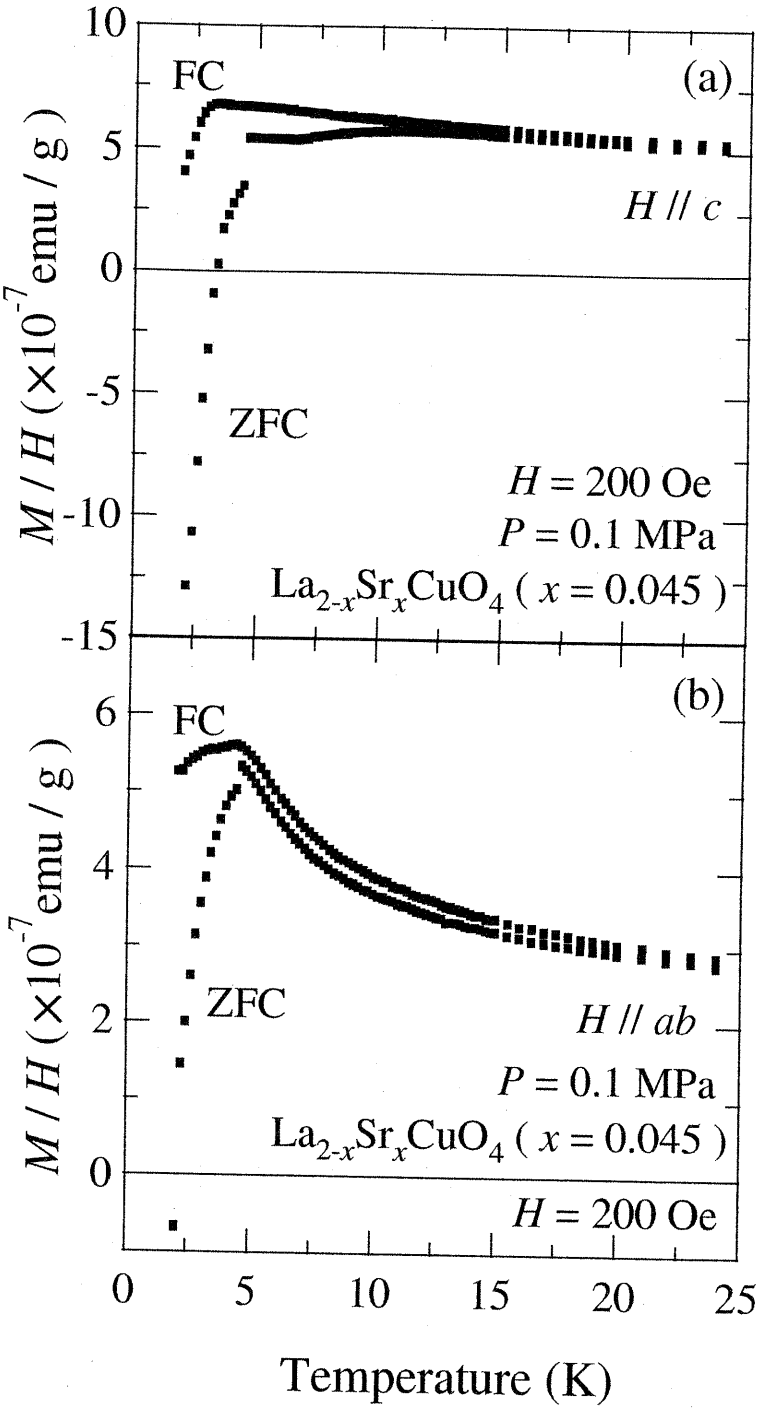

Figure 11: Temperature dependence of magnetic susceptibility at 1 T for $x = 0.045$ in the case of (a)$H//c$ and (b)$H//ab$. A hysteresis of M/H between zero field cool(ZFC) and field cool(FC) was observed below 10 K in the case of (a)$H//c$ and 5 K in the case of (b)$H//ab$. The ZFC curves suggest diamagnetism at low temperatures.

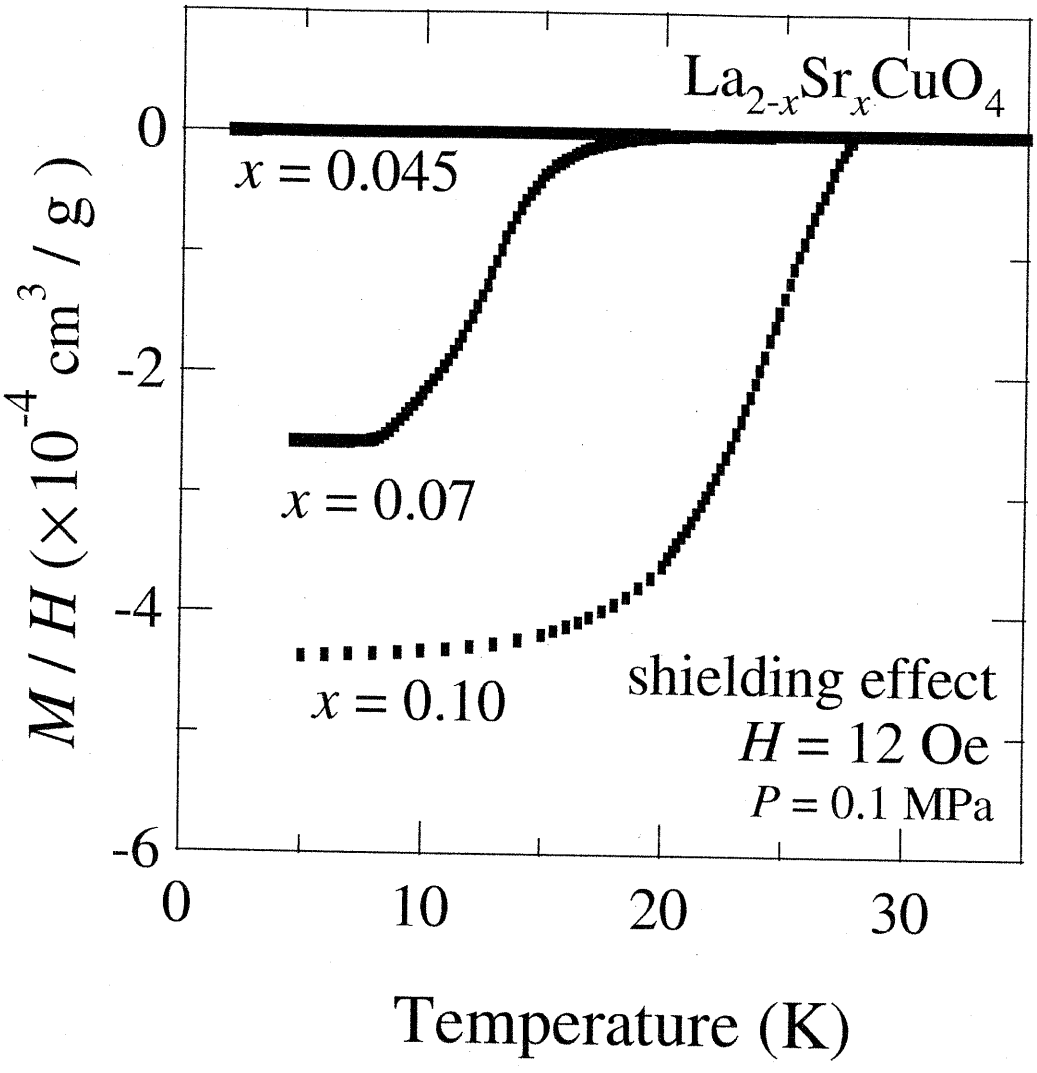

Figure 12: Shielding effect for $x = 0.045$, 0.07, and 0.1. The magnetic susceptibility is normalized by mass density. The diamagnetism seen in Fig.11 does not indicate bulk superconductivity.

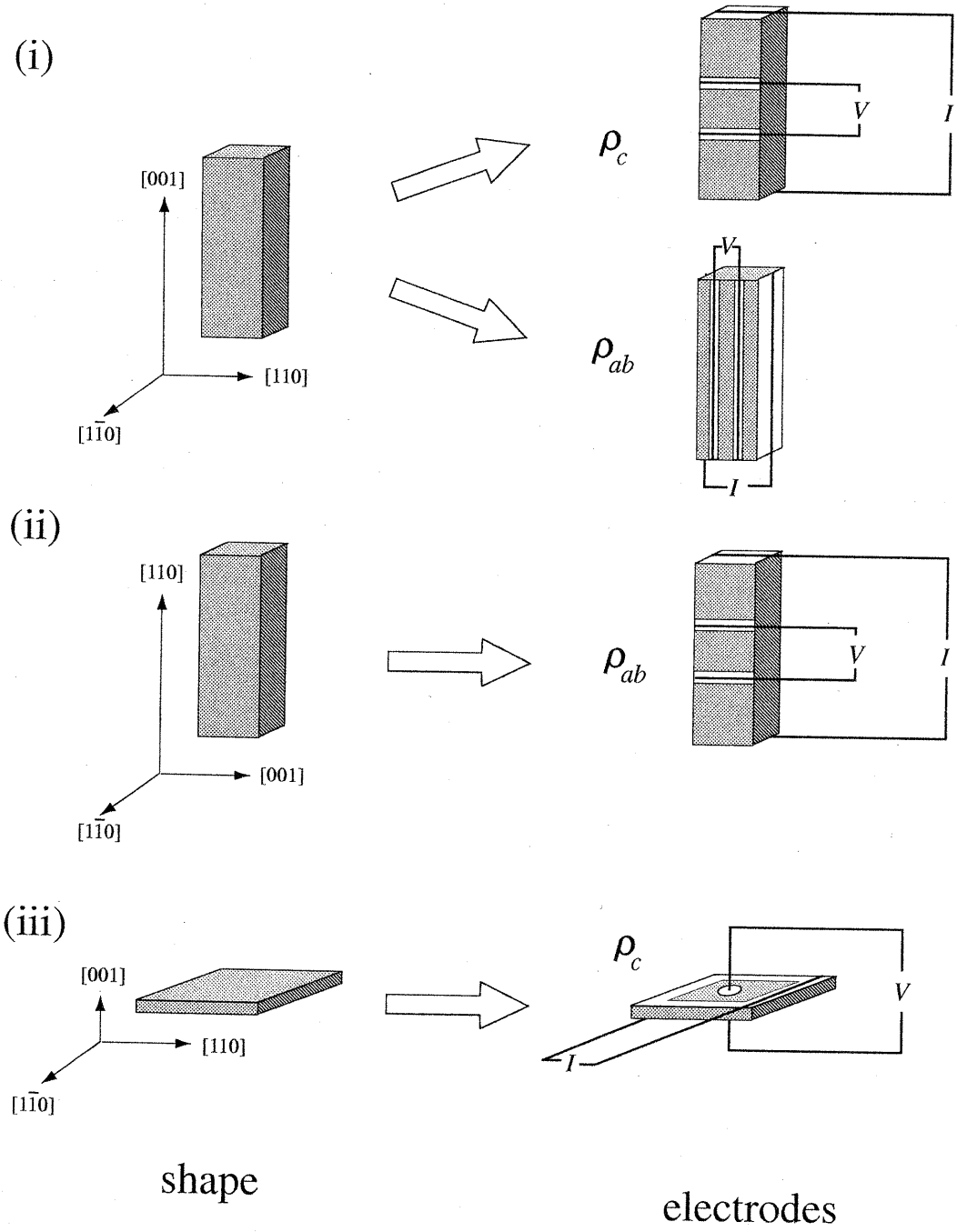

Figure 13: Schematic illustrations of sample shape and location of the electrodes. The direction of axis is shown in the tetragonal notation. The electrodes were formed by gold paste (Tokuriki Chem., 8570) with a heat treatment at 800°C for 15 minutes under flowing O_2 atmosphere.

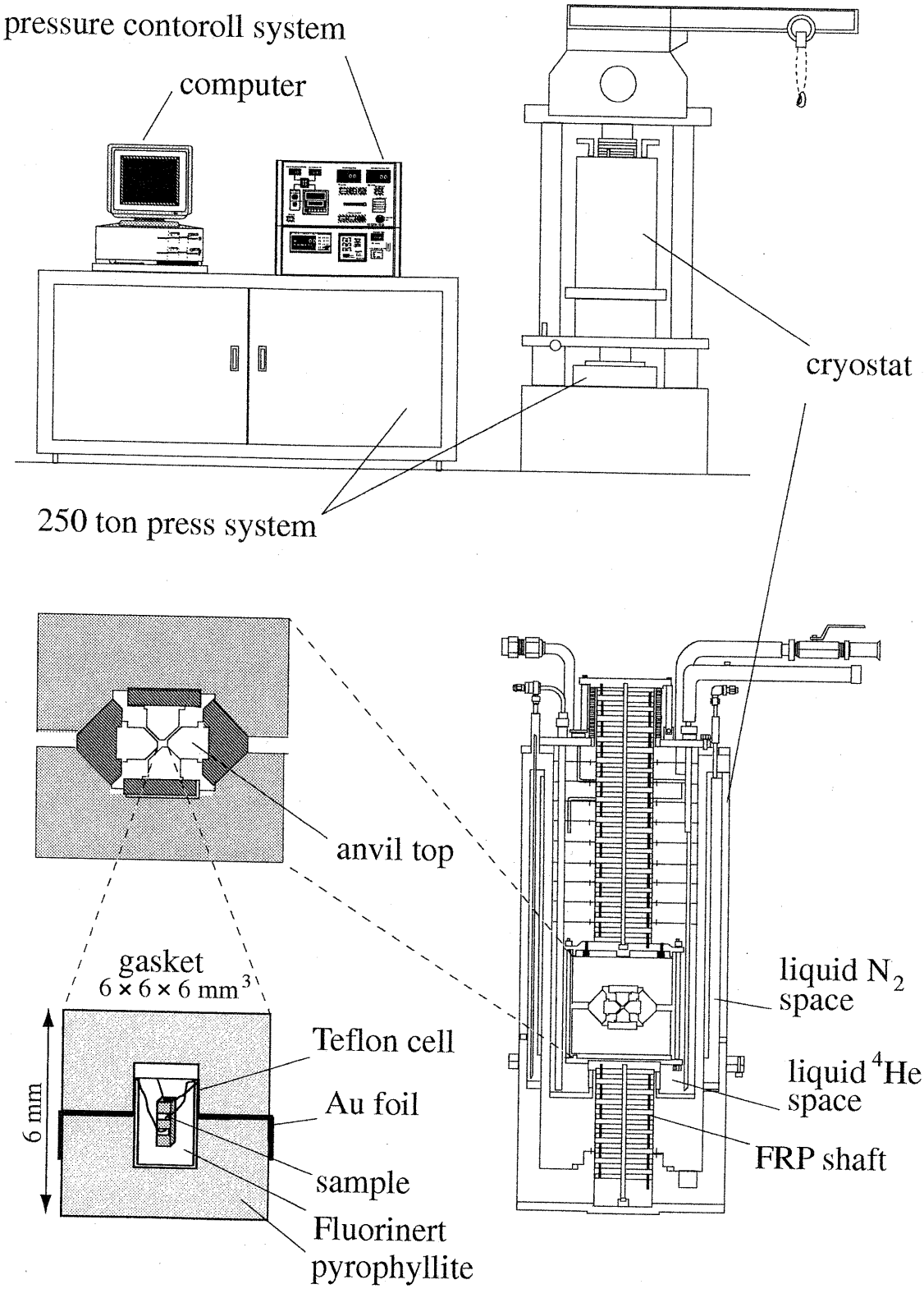

Figure 14: Schematic drawings of a cubic anvil device and a gasket.

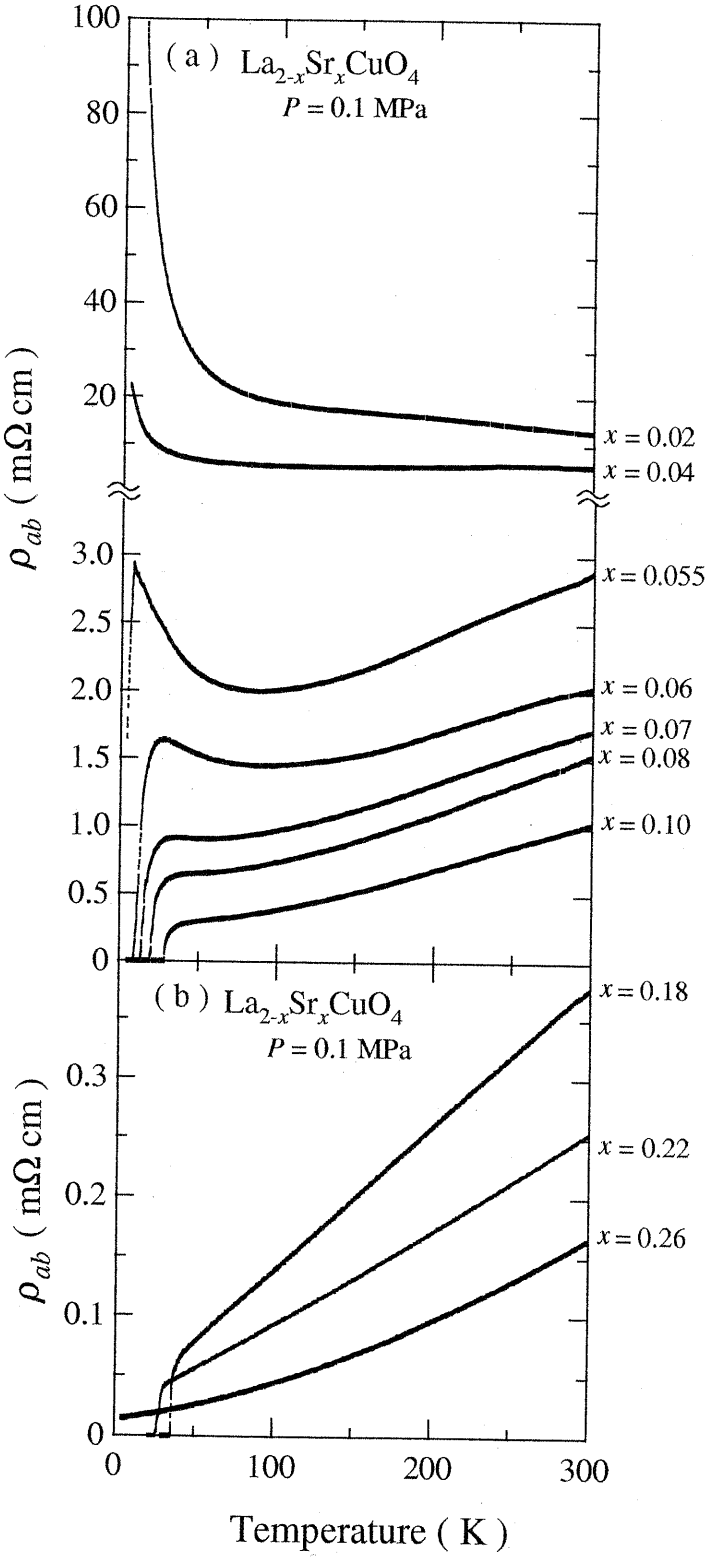

Figure 15: Temperature dependence of ρ_{ab} with various values of Sr concentration x for (a) under-doped and (b) overdoped samples at 0.1 MPa.

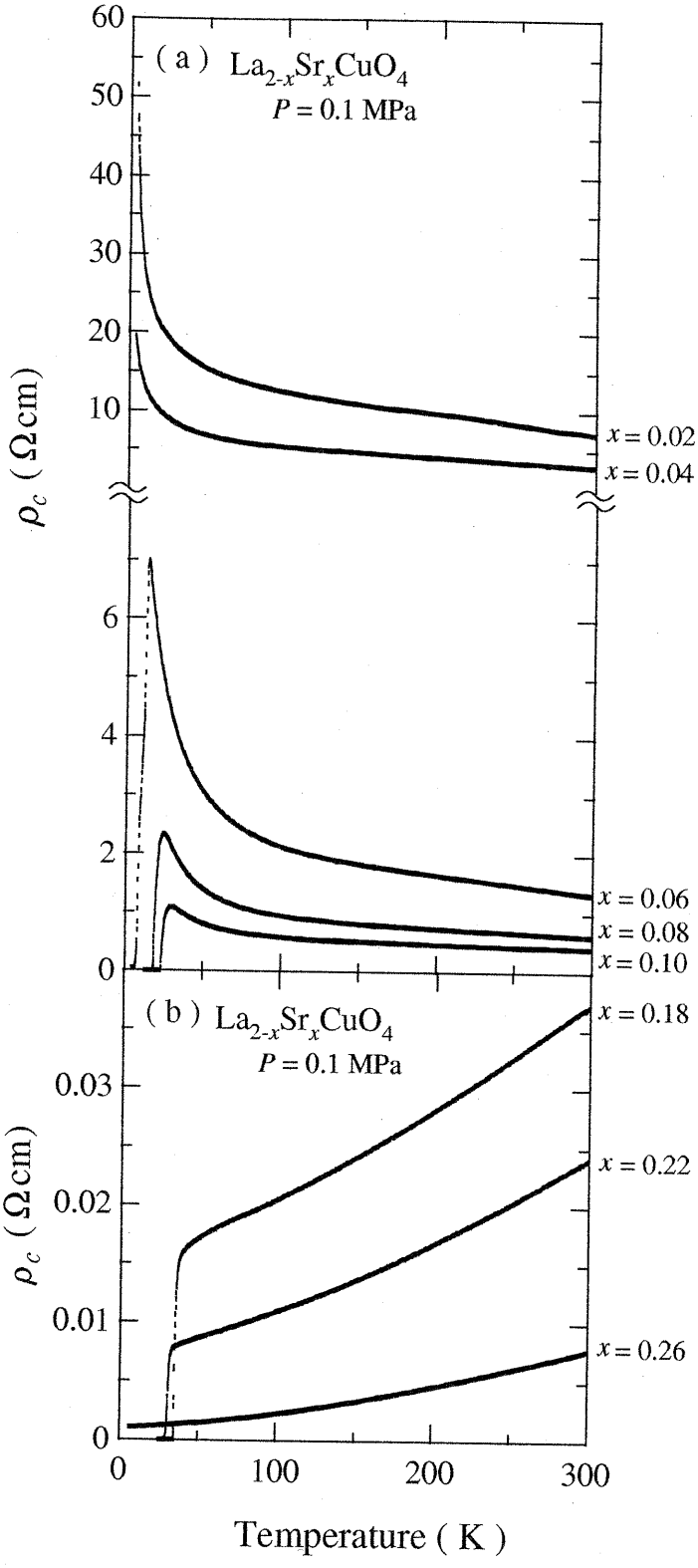

Figure 16: Temperature dependence of ρ_c with various values of Sr concentration x for (a) under-doped and (b) overdoped samples at 0.1 MPa.

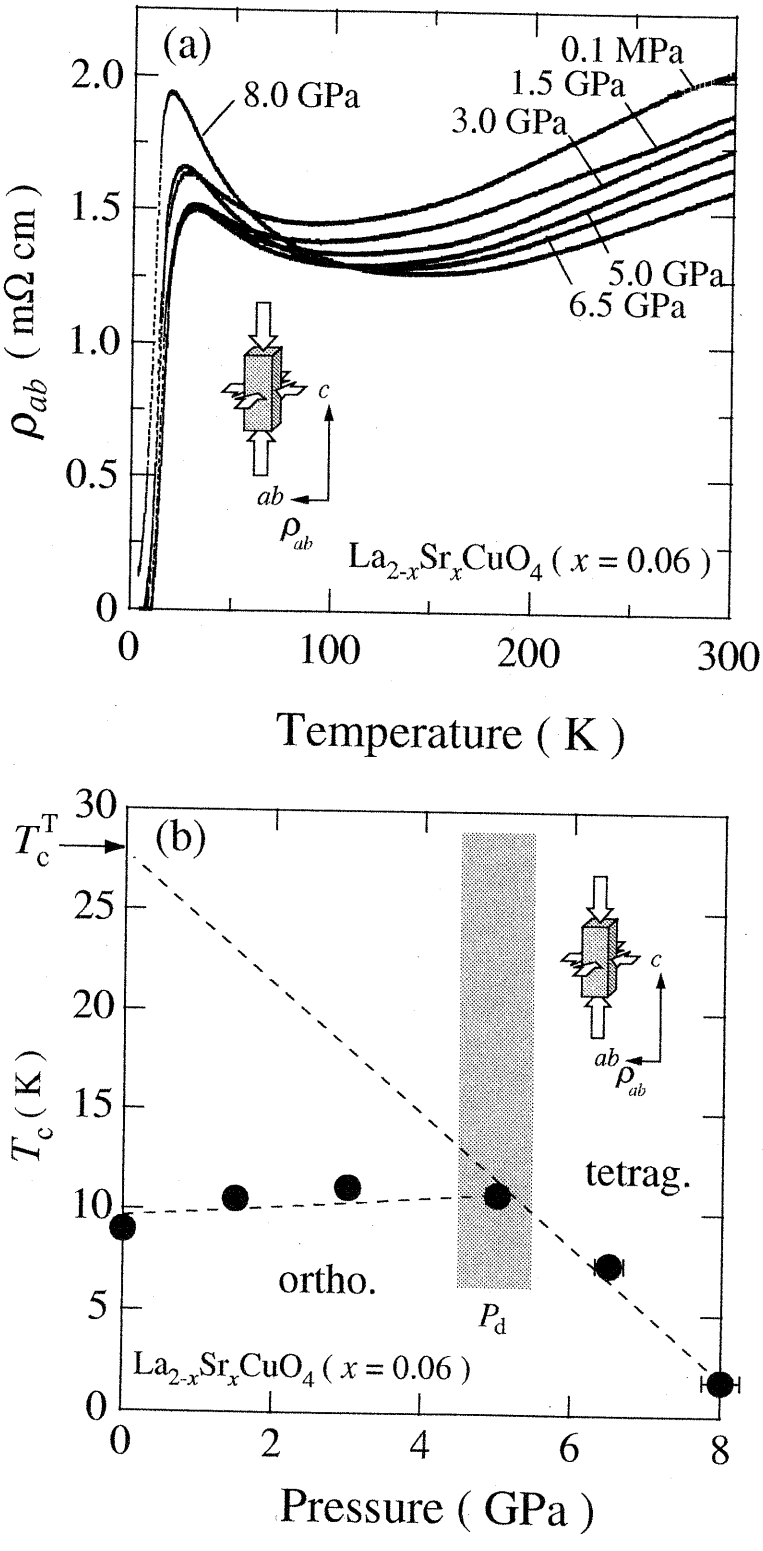

Figure 17: (a) Temperature dependence of ρ_{ab} under pressure and (b) pressure dependence of T_c for $x = 0.06$.

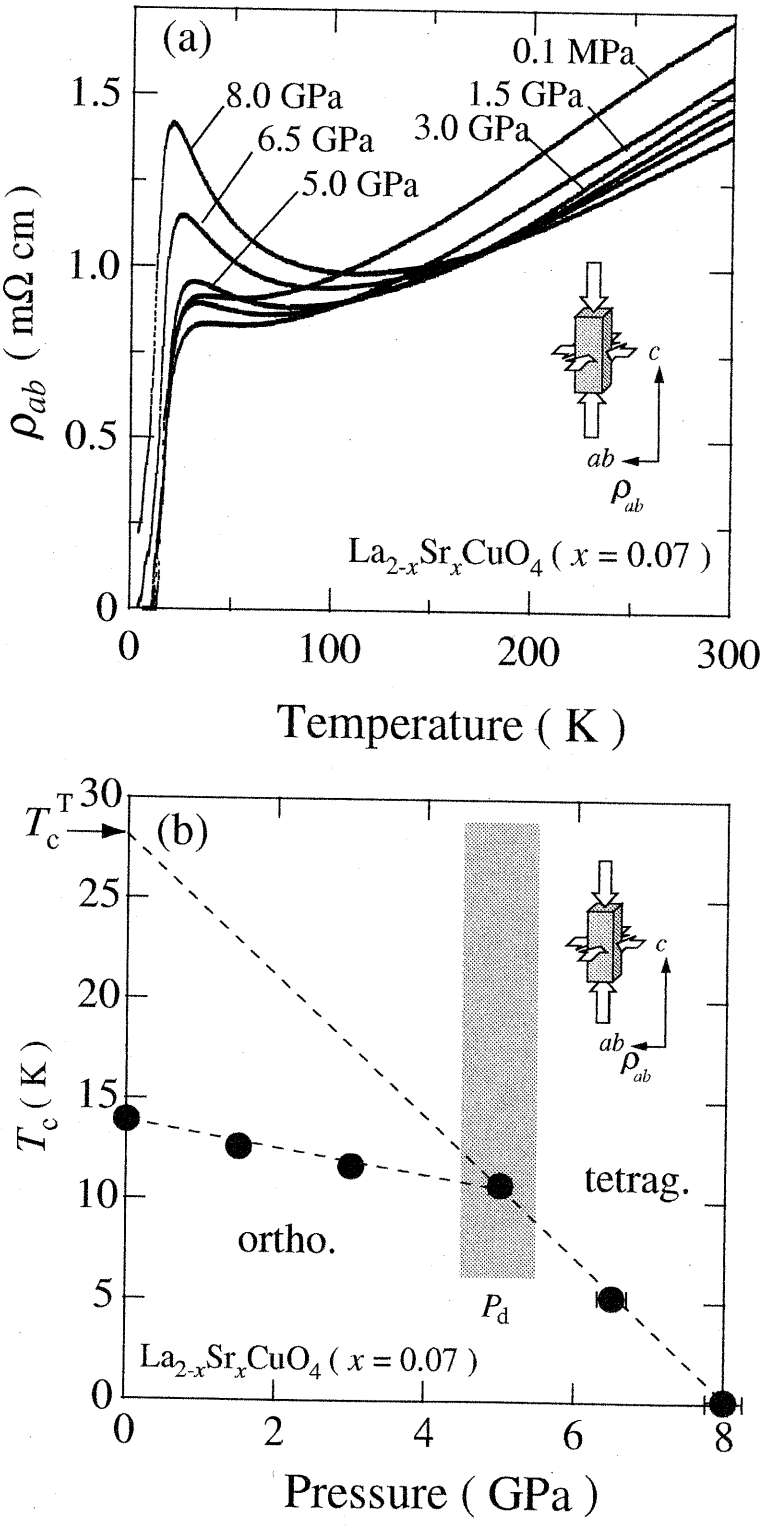

Figure 18: (a) Temperature dependence of ρ_{ab} under pressure and (b) pressure dependence of T_c for $x = 0.07$.

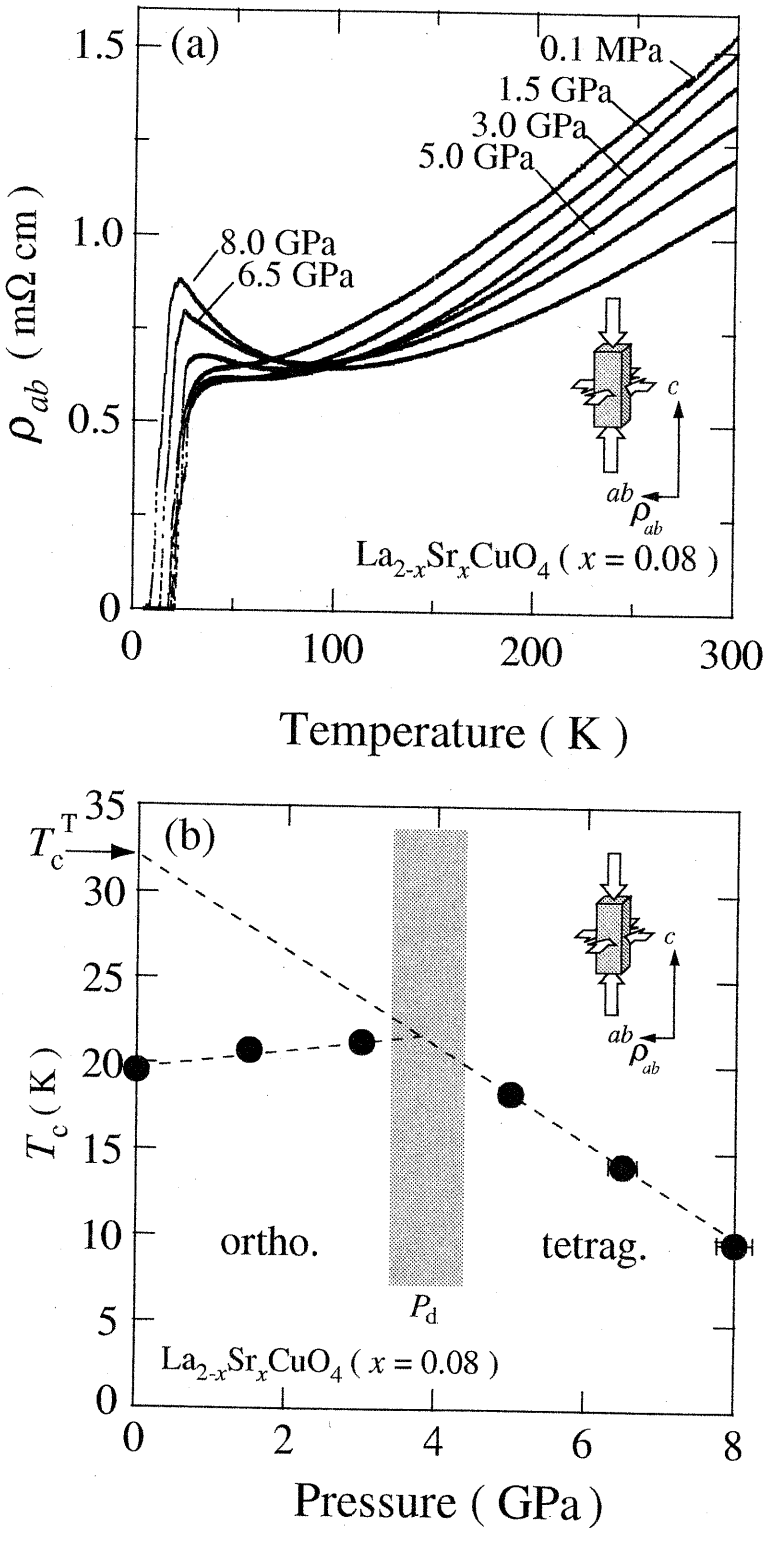

Figure 19: (a) Temperature dependence of ρ_{ab} under pressure and (b) pressure dependence of T_c for $x = 0.08$.

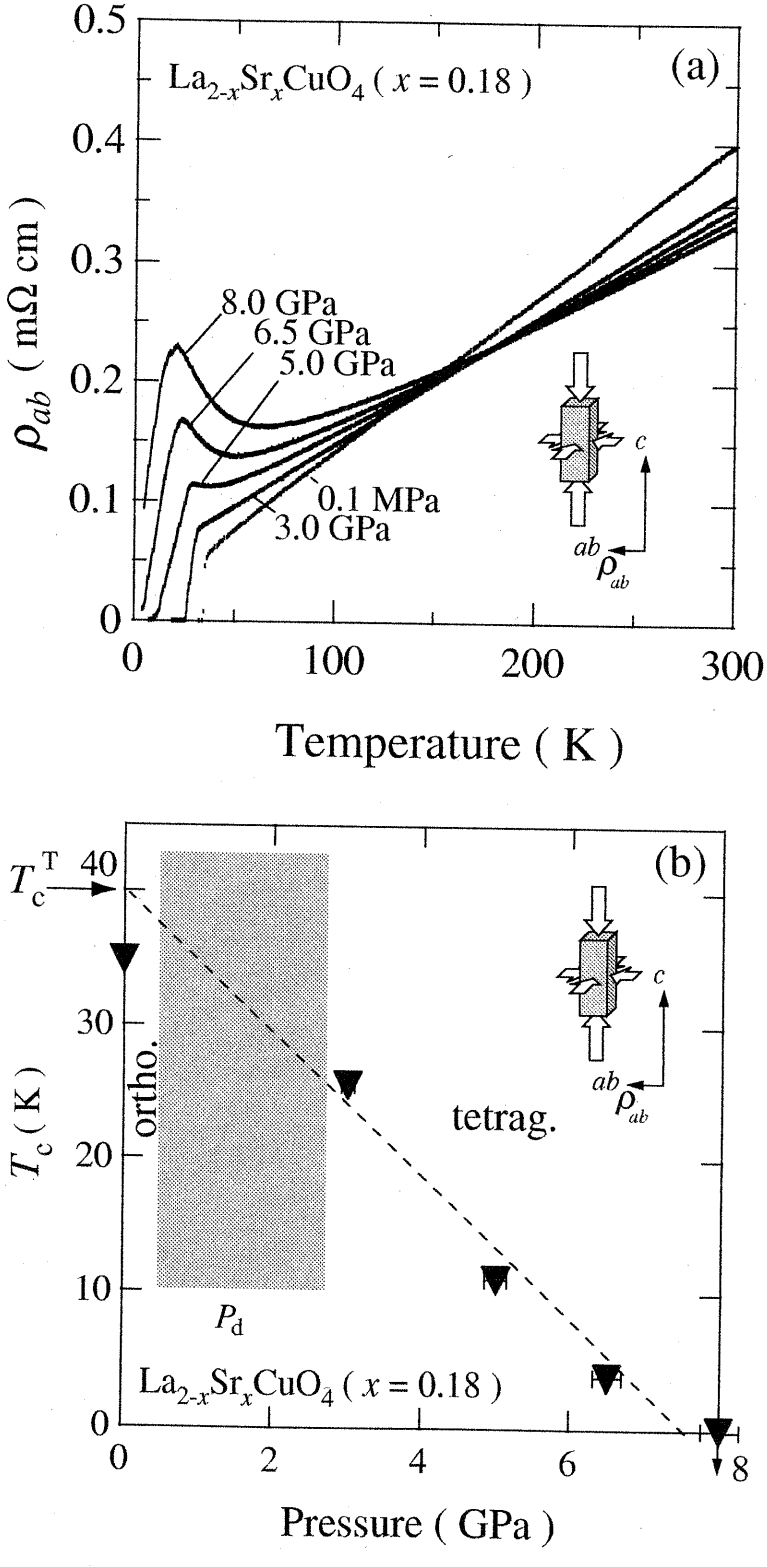

Figure 20: (a) Temperature dependence of ρ_{ab} under pressure and (b) pressure dependence of T_c for $x = 0.18$.

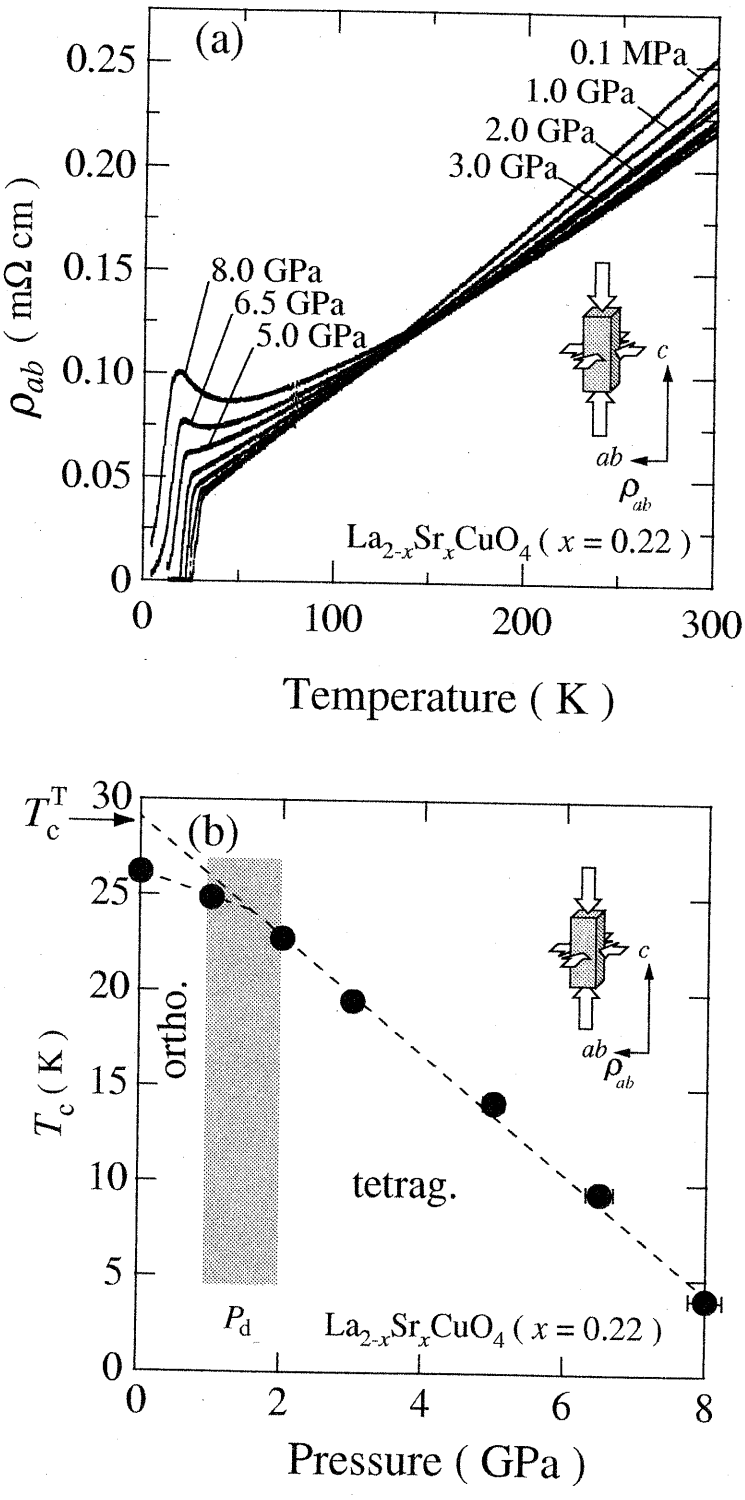

Figure 21: (a) Temperature dependence of ρ_{ab} under pressure and (b) pressure dependence of T_c for $x = 0.22$.

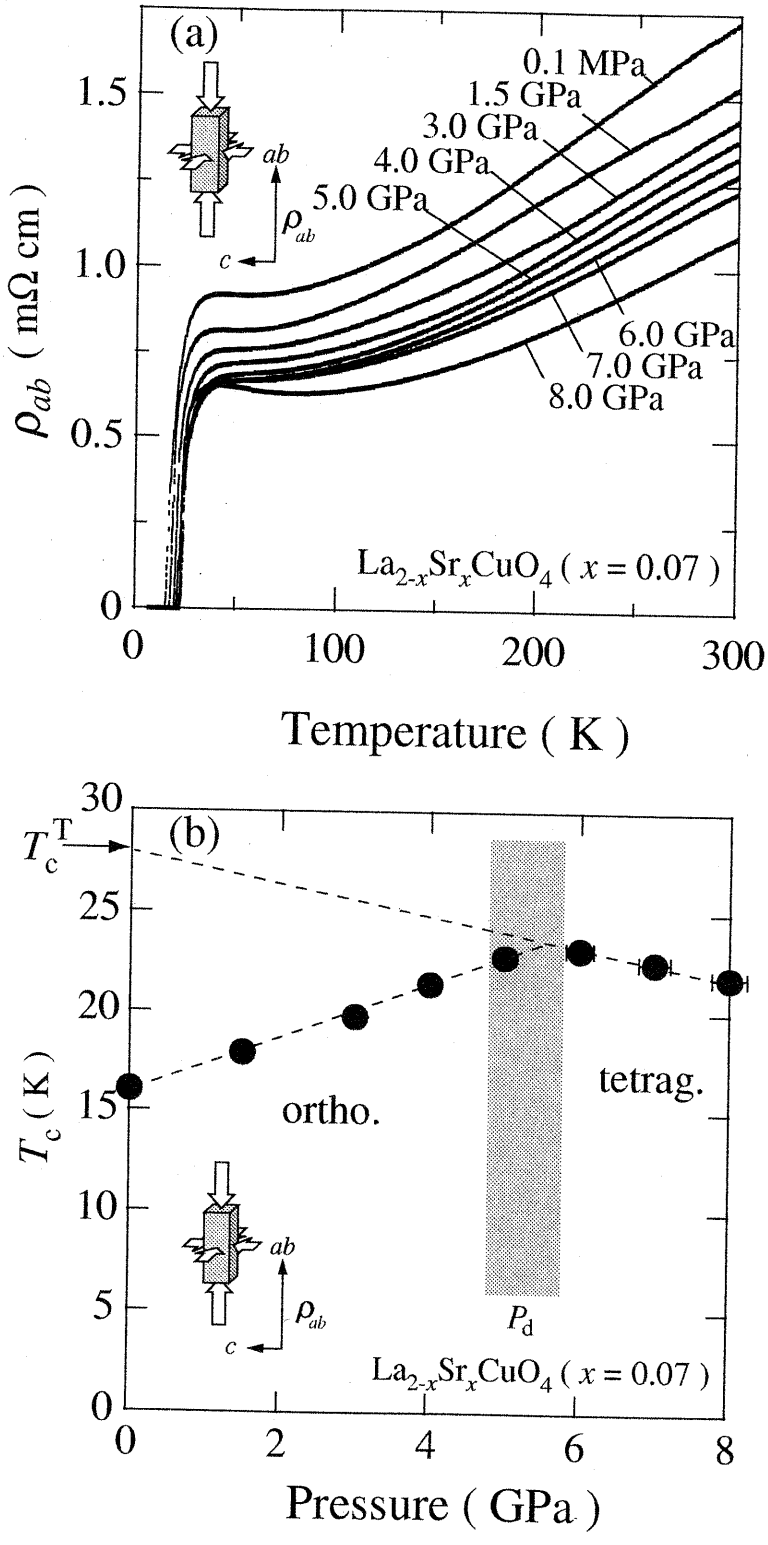

Figure 22: (a) Temperature dependence of ρ_{ab} under pressure and (b) pressure dependence of T_c for $x = 0.07$.

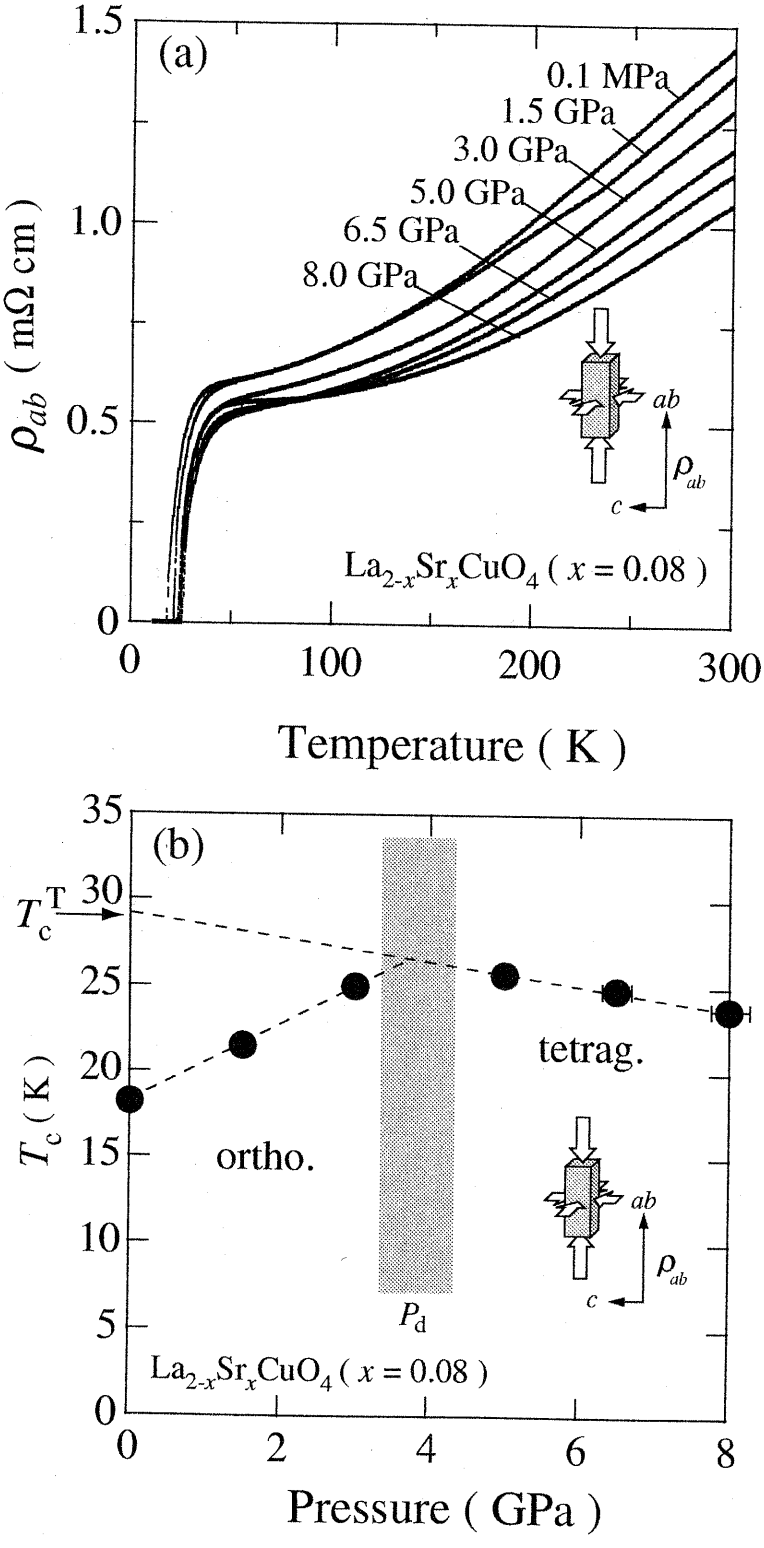

Figure 23: (a) Temperature dependence of ρ_{ab} under pressure and (b) pressure dependence of T_c for $x = 0.08$.

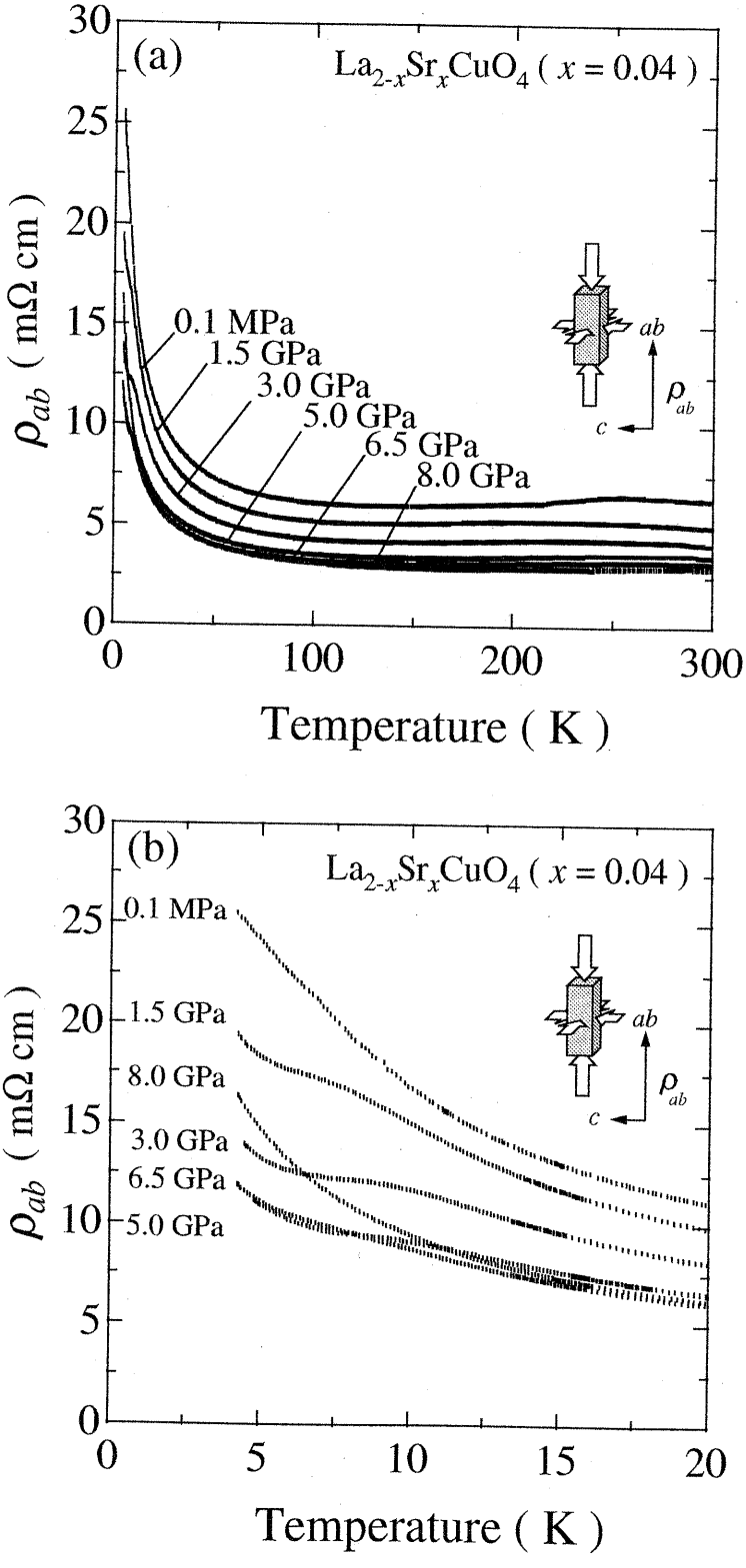

Figure 24: Temperature dependence of ρ_{ab} under pressure (a) from $T = 4.2$ K to 300 K and (b) from $T = 4.2$ K to 20 K.

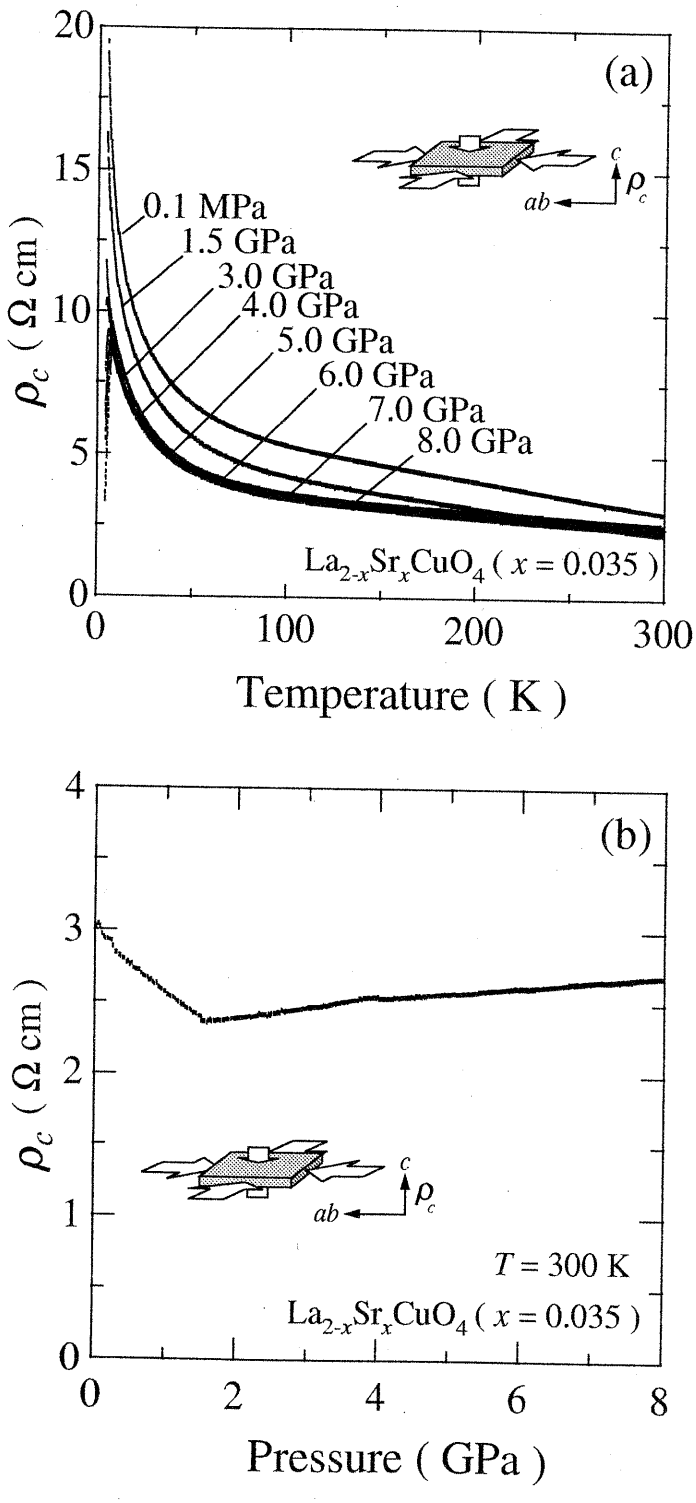

Figure 25: (a) Temperature dependence of ρ_{ab} under pressure and (b) pressure dependence of ρ_{ab} at 300 K for $x = 0.035$.

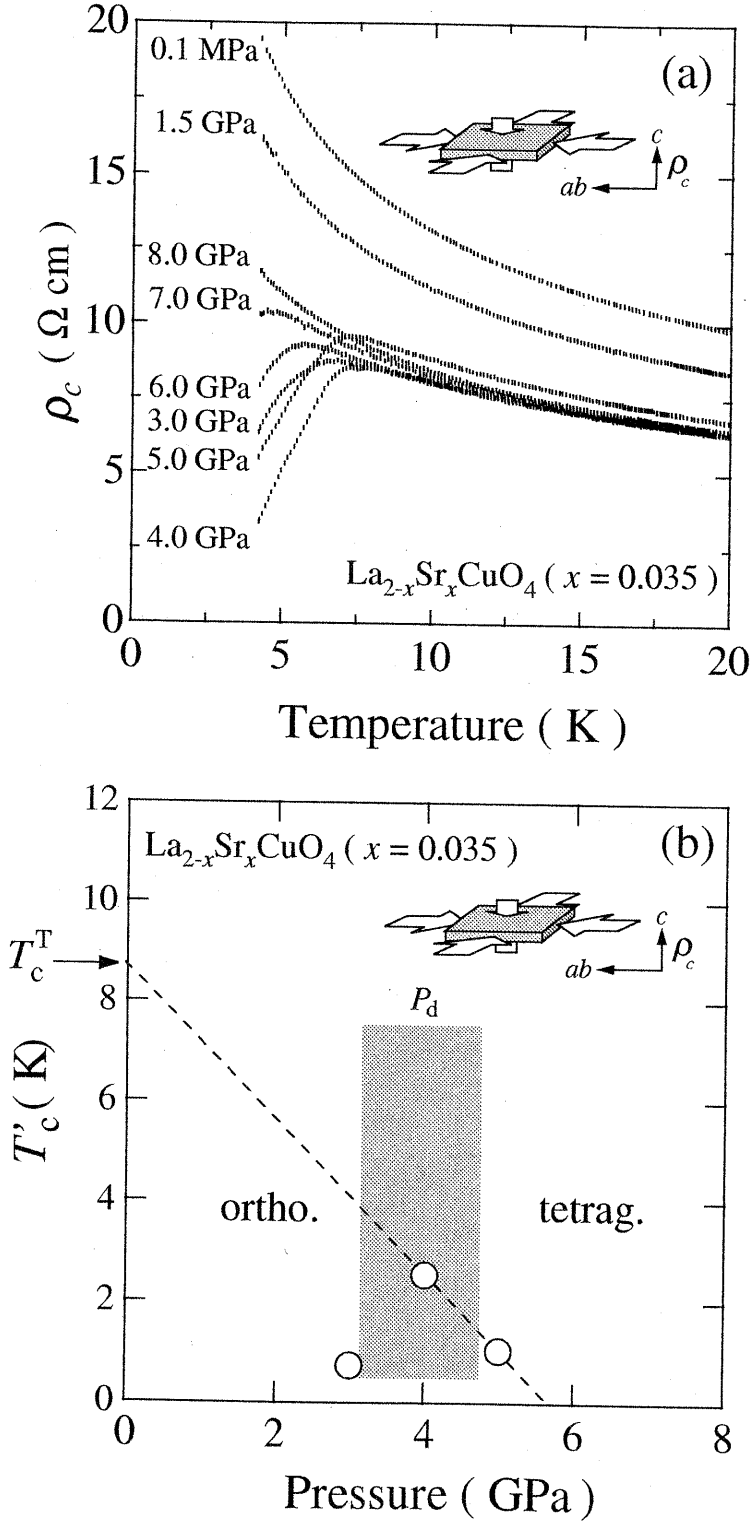

Figure 26: (a) Temperature dependence of ρ_{ab} under pressure at low temperatures and (b) pressure dependence of T_c' which is determined by extrapolation of drop of ρ_c to $\rho_c = 0$ for $x = 0.035$.

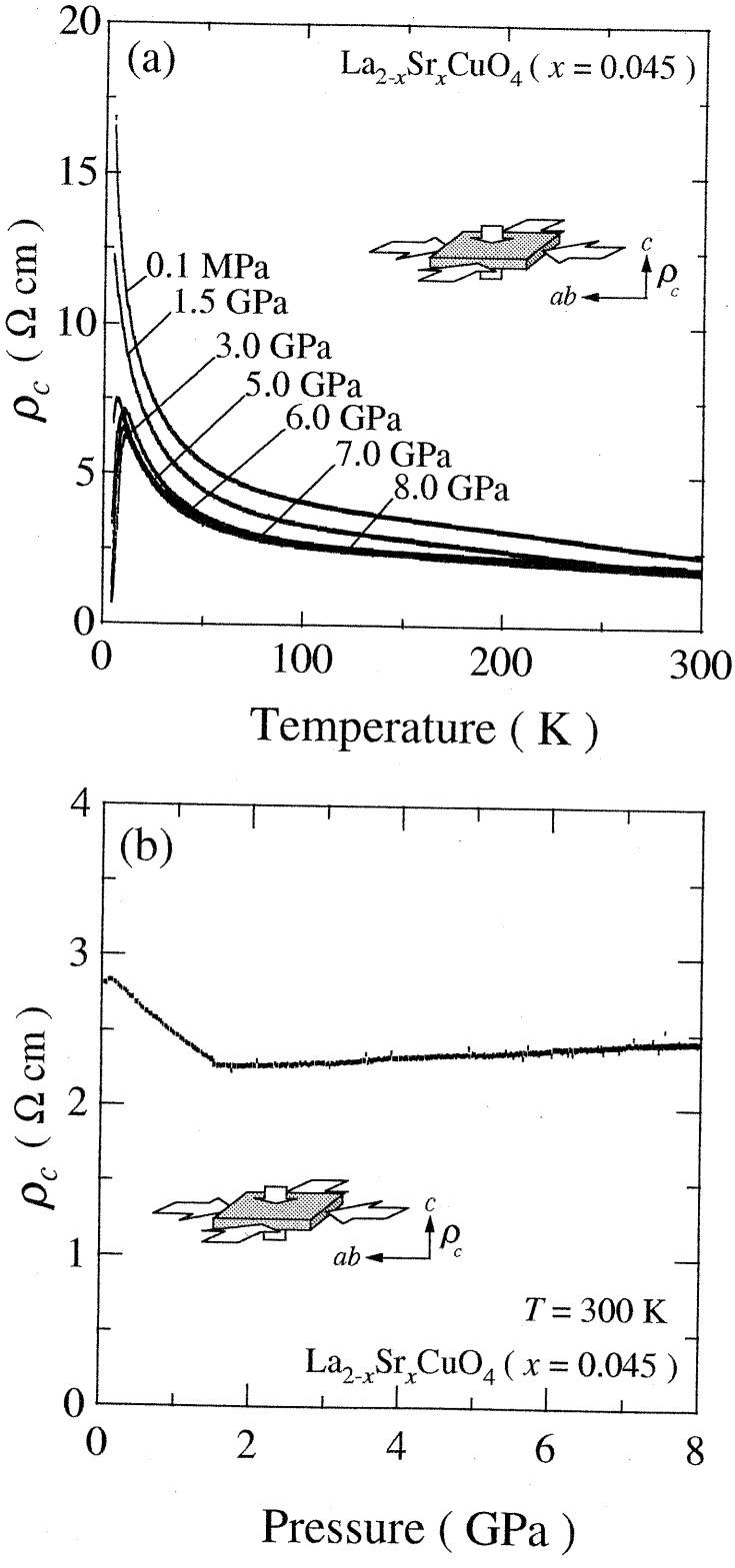

Figure 27: (a) Temperature dependence of ρ_{ab} under pressure and (b) pressure dependence of ρ_{ab} at 300 K for $x = 0.045$.

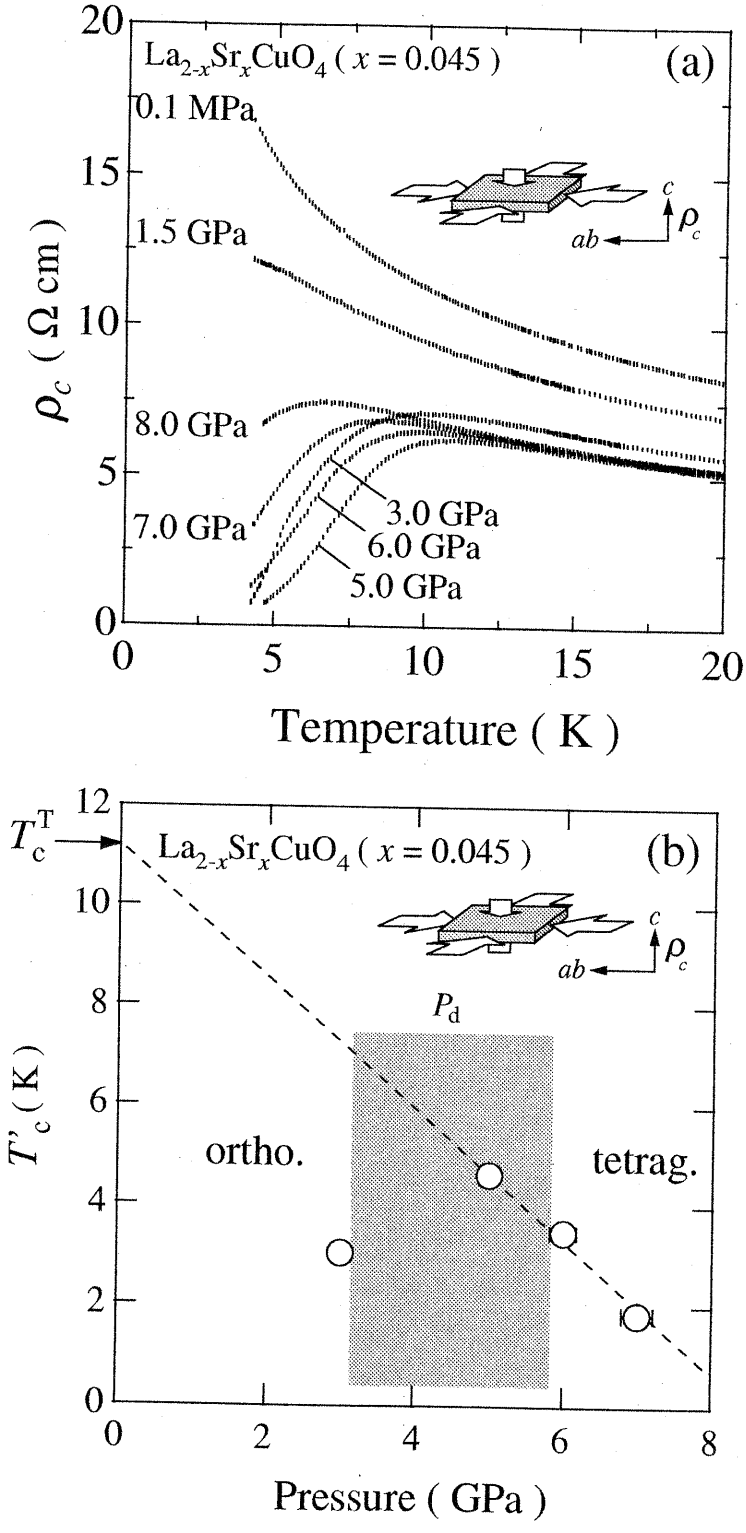

Figure 28: (a) Temperature dependence of ρ_{ab} under pressure at low temperatures and (b) pressure dependence of T_c' which is determined by extrapolation of drop of ρ_c to $\rho_c = 0$ for $x = 0.045$.

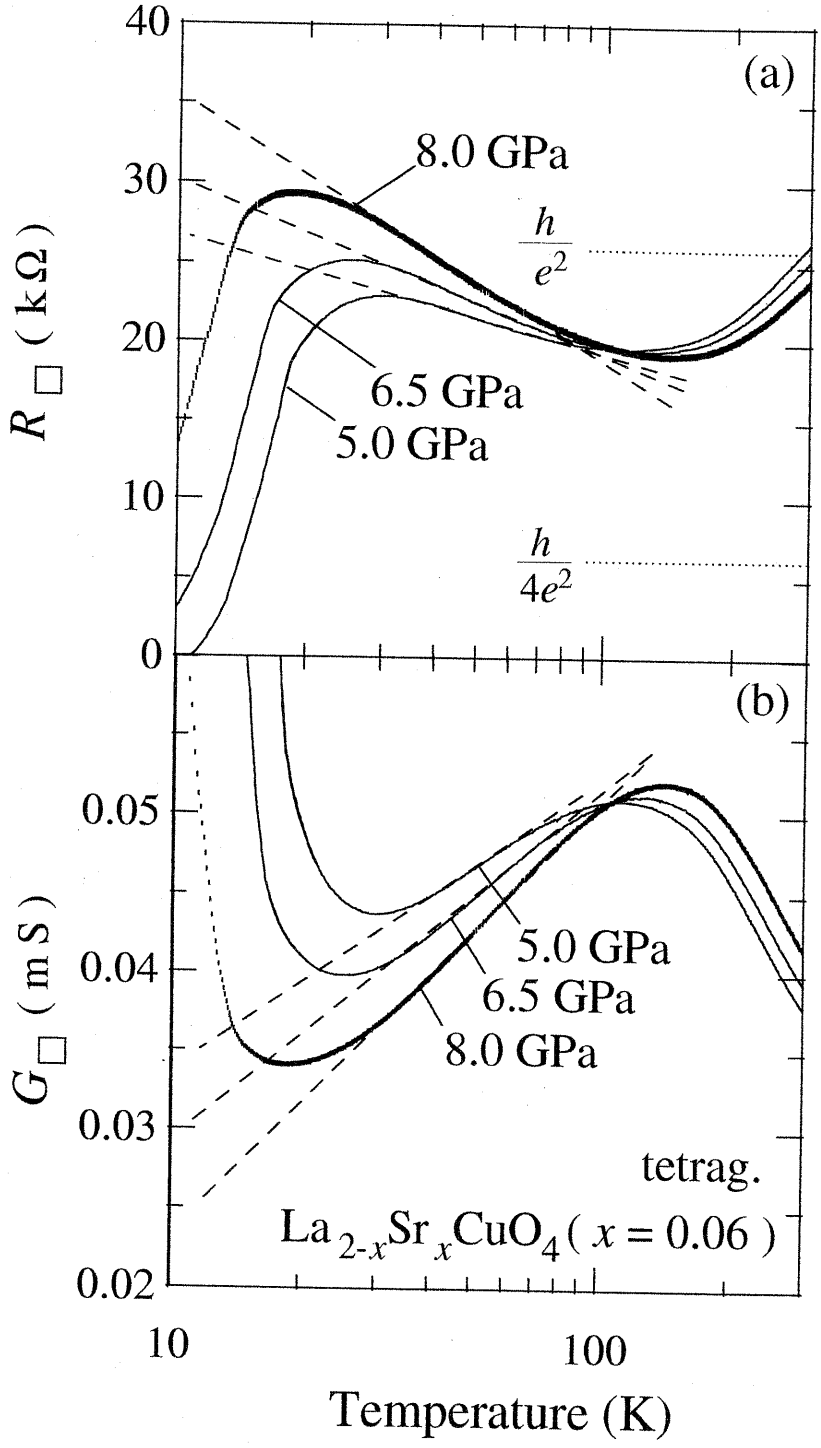

Figure 29: Temperature dependence of (a) resistance $R_\square$ and (b) conductance $G_\square$ per CuO_2 plane in the tetragonal phase for $x = 0.06$. $R_\square$ and $G_\square$ depend linearly on $\ln T$ in a wide range of low temperatures. The broken lines are guides for the eyes.

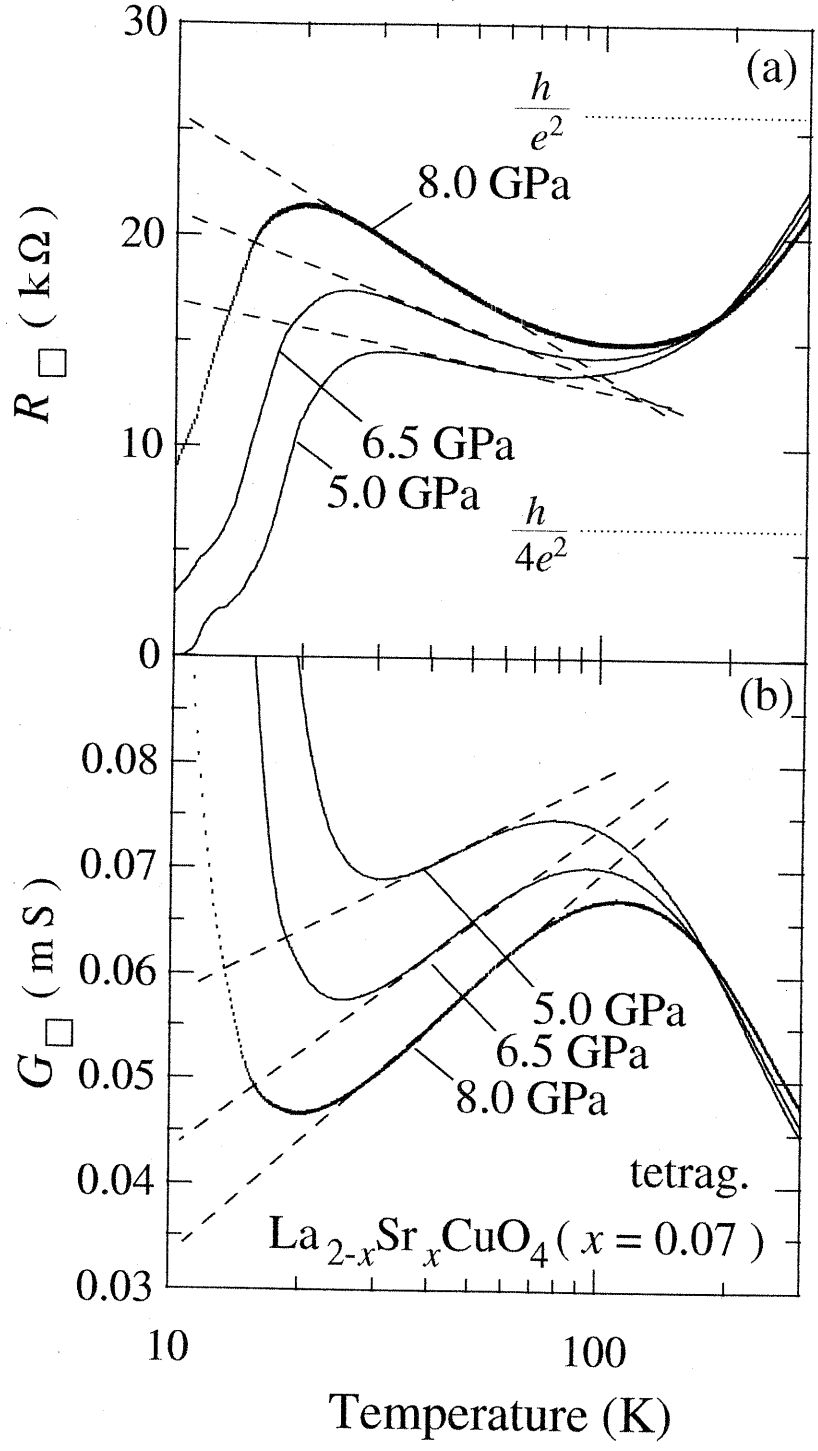

Figure 30: Temperature dependence of (a) resistance $R_\square$ and (b) conductance per CuO_2 plane in the tetragonal phase for $x = 0.07$. $R_\square$ and $G_\square$ depend linearly on $\ln T$ in a wide range of low temperatures. The broken lines are guides for the eyes.

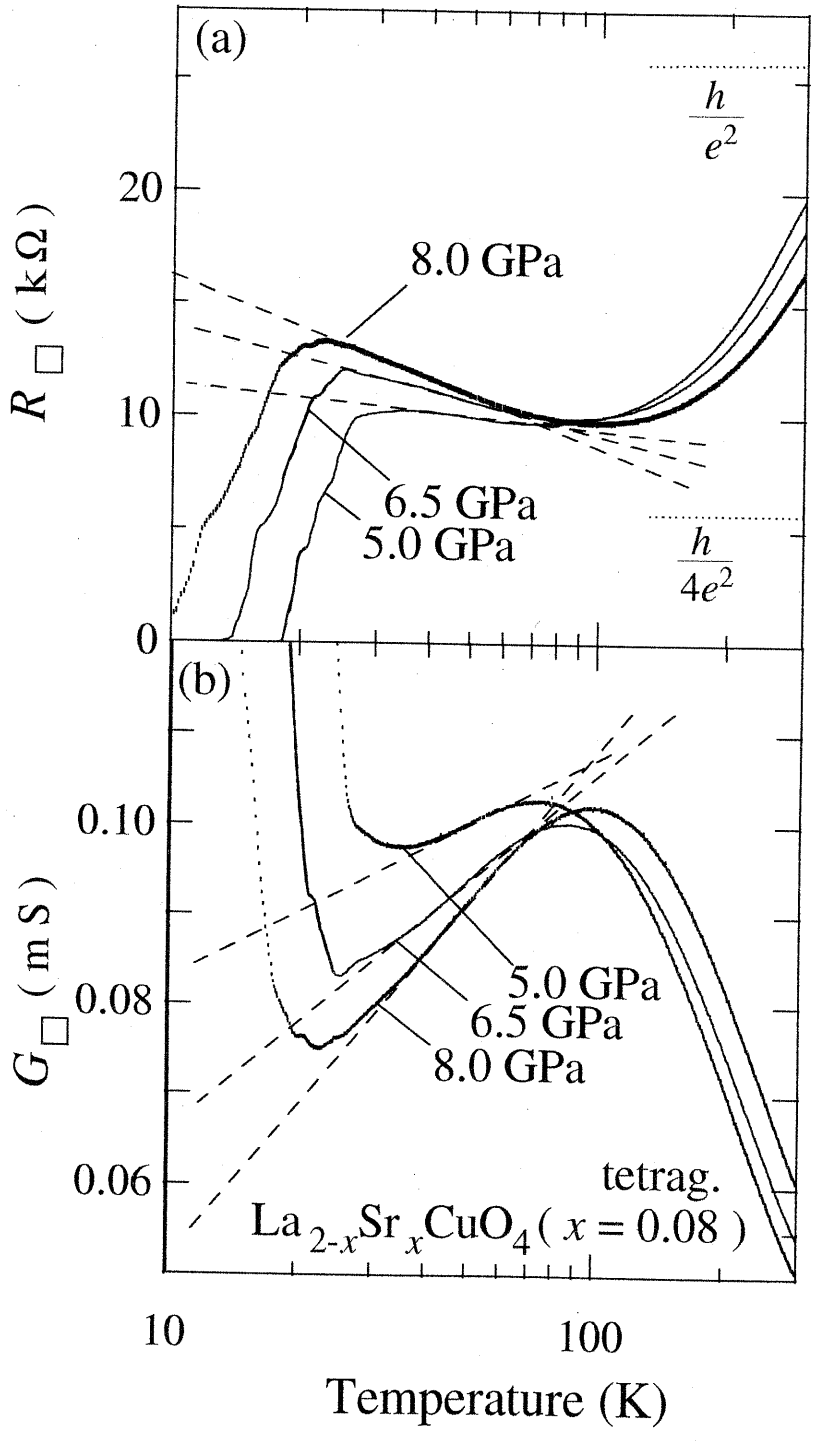

Figure 31: Temperature dependence of (a) resistance $R_\square$ and (b) conductance $G_\square$ per CuO_2 plane in the tetragonal phase for $x = 0.08$. $R_\square$ and $G_\square$ dependent linearly on $\ln T$ in a wide range of low temperatures. The broken lines are guides for the eyes.

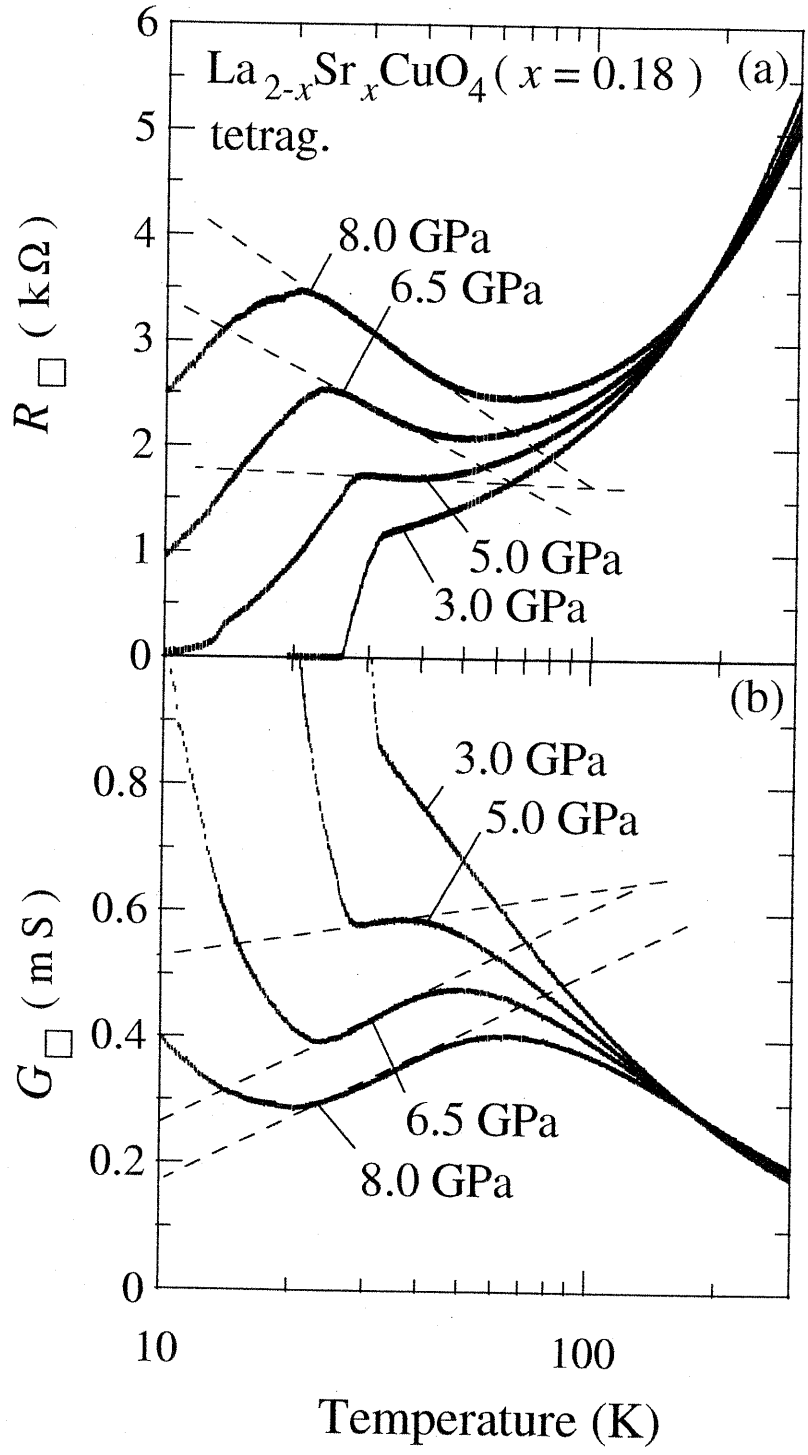

Figure 32: Temperature dependence of (a) resistance $R_\square$ and (b) conductance $G_\square$ per CuO_2 plane in the tetragonal phase for $x = 0.18$. The temperature range of the linear dependence on $\ln T$ of $R_\square$ and $G_\square$ is narrow compared with under-doped samples. The broken lines are guides for the eyes.

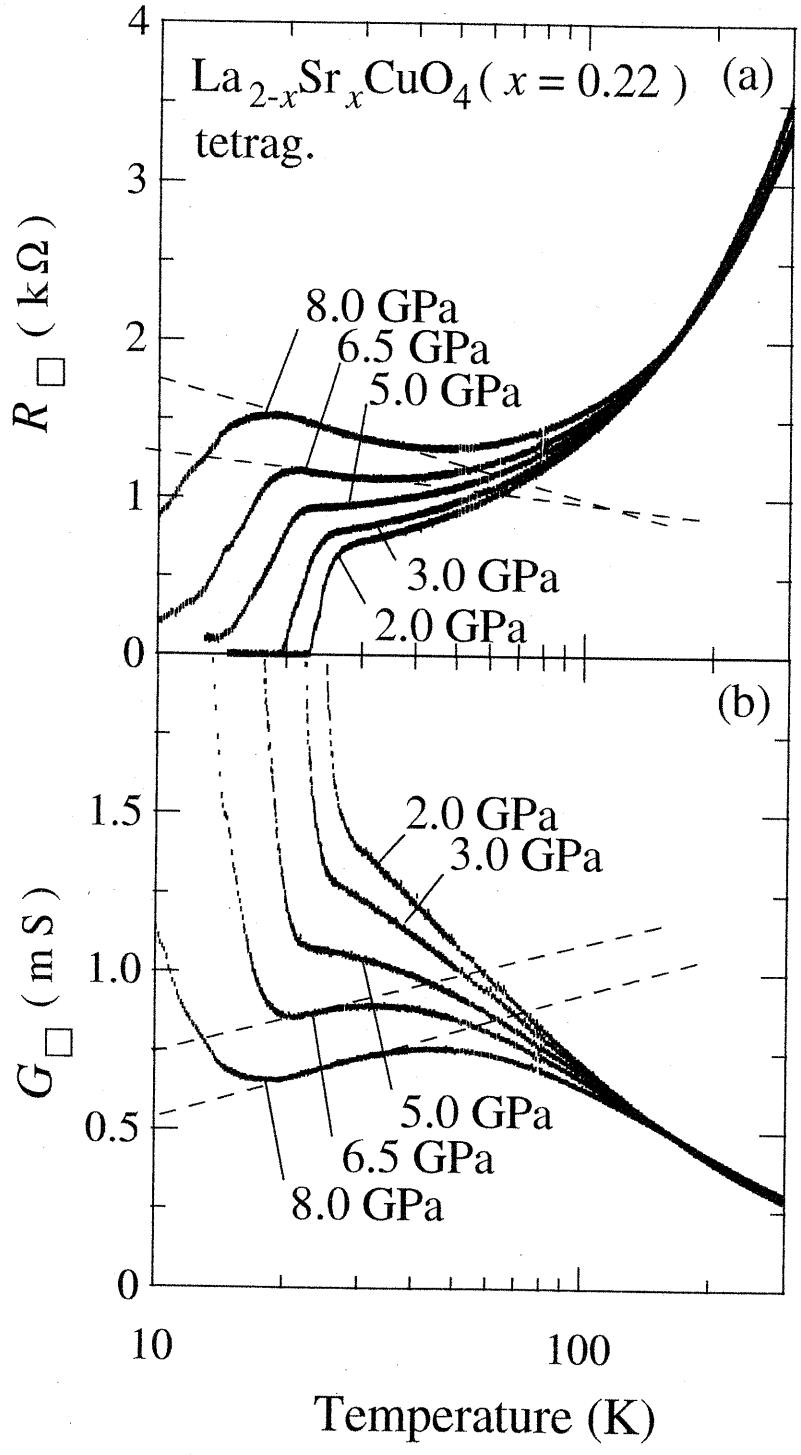

Figure 33: Temperature dependence of (a) resistance $R_\square$ and (b) conductance $G_\square$ per CuO_2 plane in the tetragonal phase for $x = 0.22$. The temperature range of the linear dependence on $\ln T$ of $R_\square$ and $G_\square$ is narrow compared with under-doped samples. The broken lines are guides for the eyes.

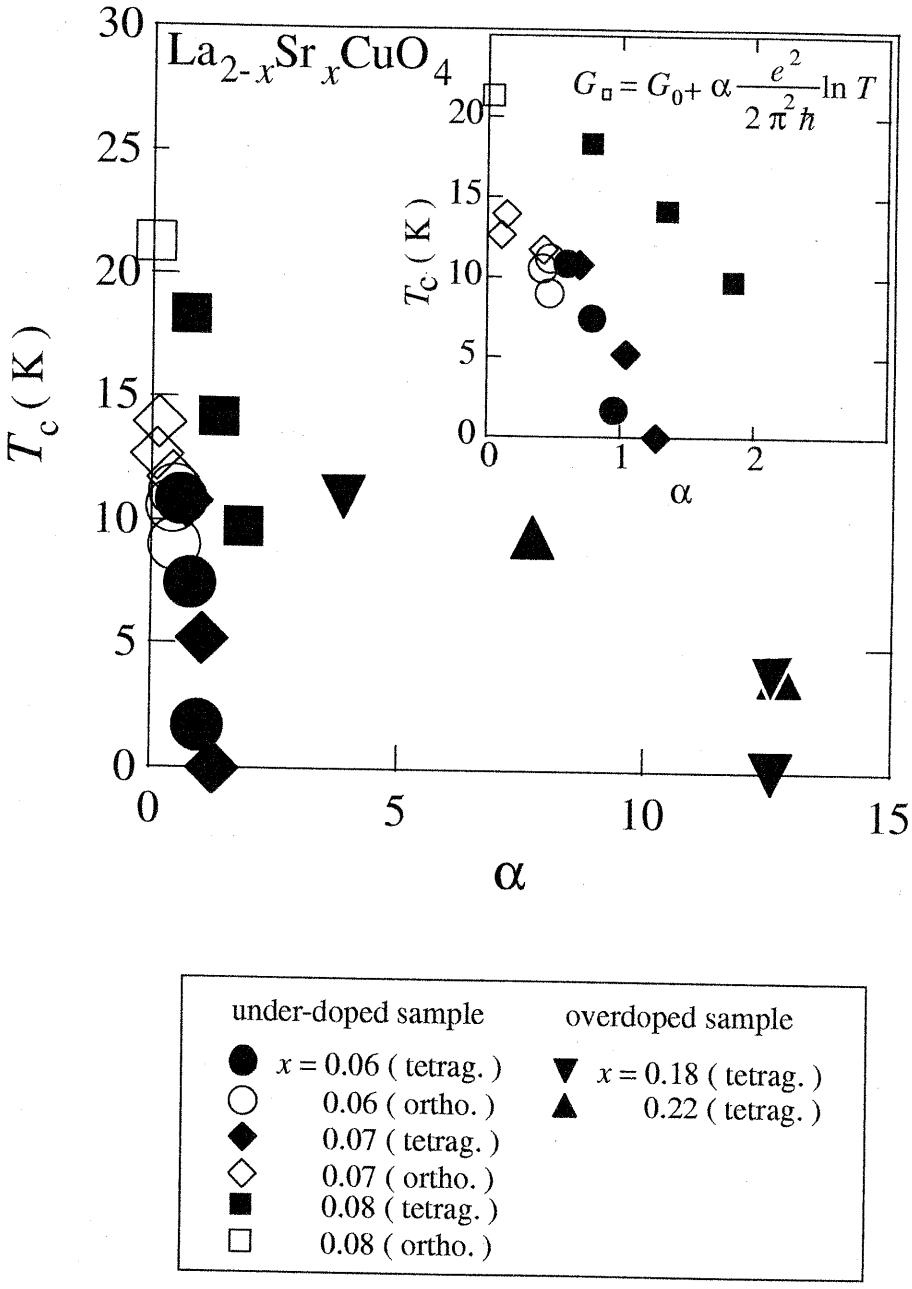

Figure 34: Plots of T_c against α which is the prefactor of $\ln T$ normalized by $e^2/(2\pi^2\hbar)$. The plots for $x = 0.18$ and 0.22 deviate from those for under-doped samples. The inset shows the plot of T_c vs. α in the under-doped samples. In the under-doped samples, superconducting-insulating phase transition occurs around $\alpha = 1 \sim 3$ which is often observed in the weak localization materials.[23),24)]

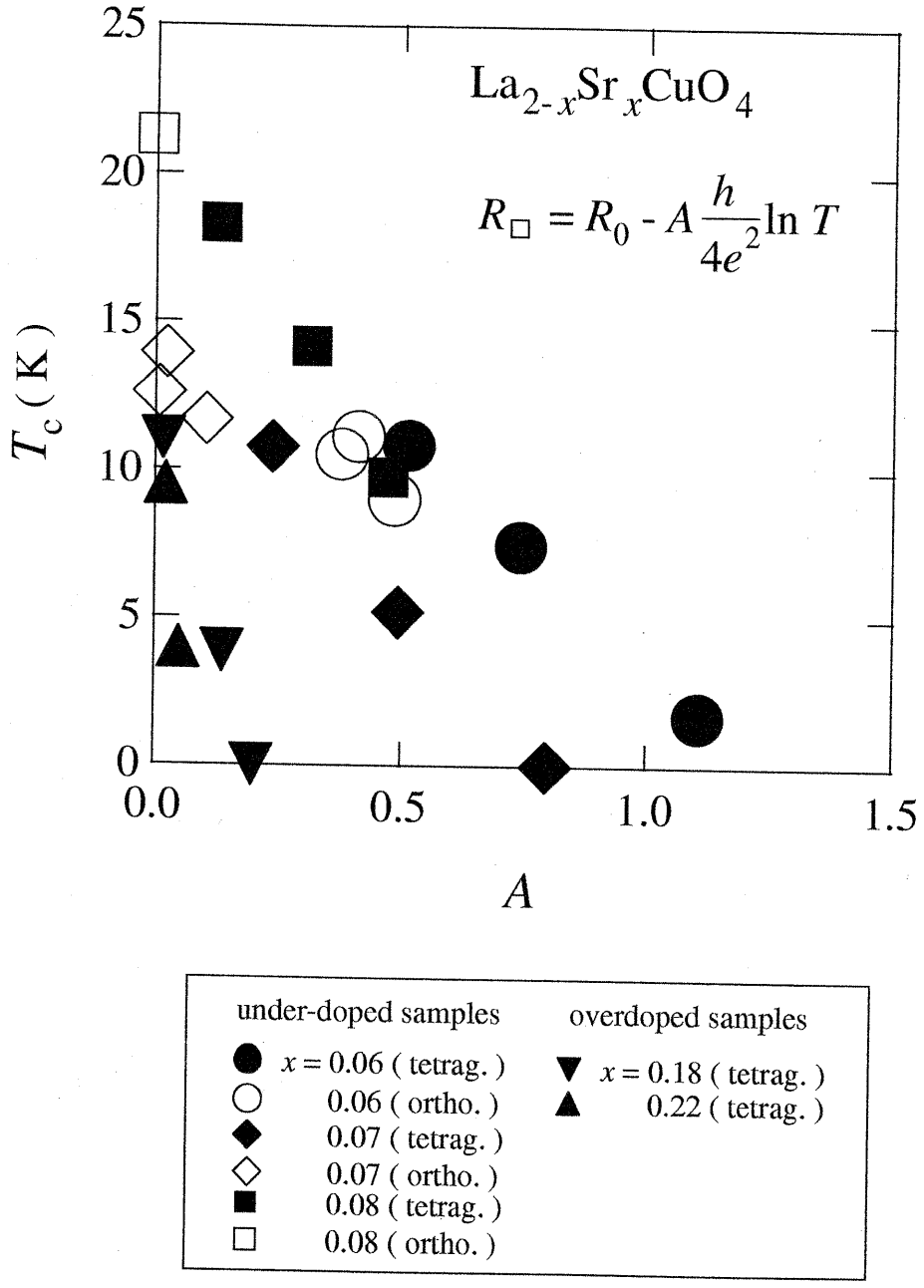

Figure 35: The normalized slope A of $R_\square$ against $\ln T$ plotted as a function of T_c. In the under-doped samples, superconducting-insulating phase transition occurs around $A = 1$ which is close to the universal critical sheet resistance[22] observed in the ultrathin film systems.

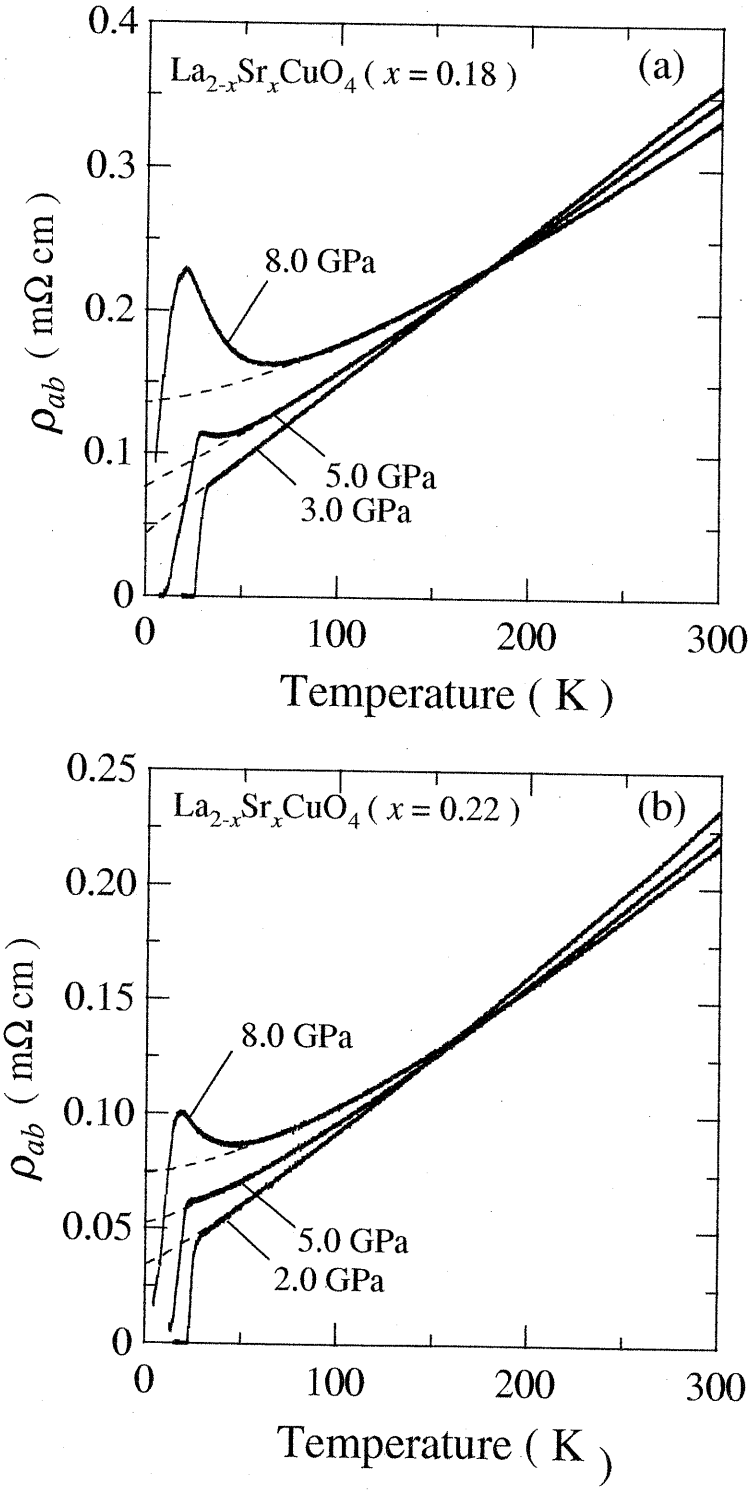

Figure 36: The best fittings of ρ_{ab} by $\rho_{ab} = \rho_0 + \beta T^n$ (a) at 3.0, 5.0 and 8.0 GPa for $x = 0.18$ and (b) at 2.0, 5.0 and 8.0 GPa for $x = 0.22$. The fitting lines are indicated by the broken lines.

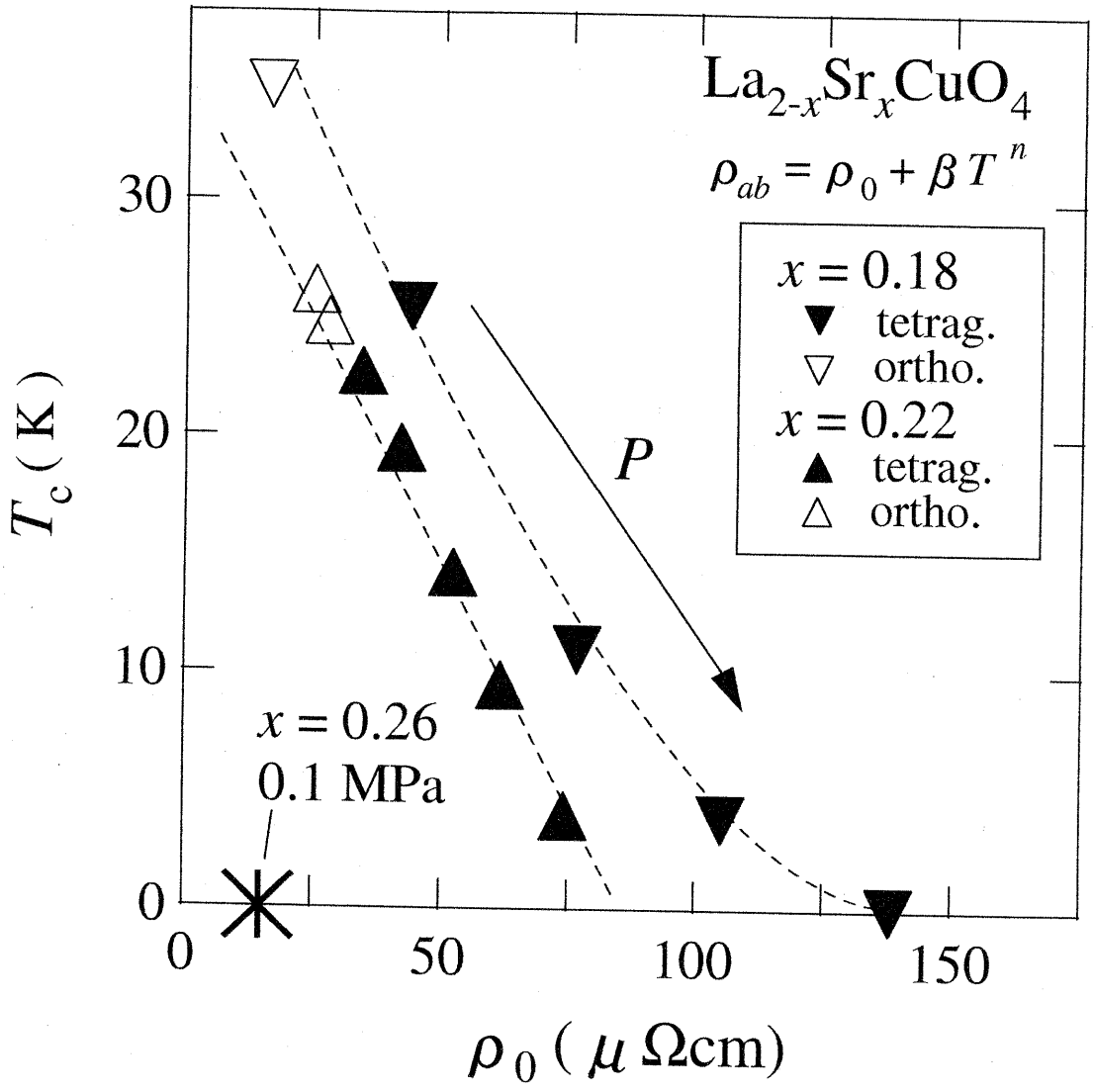

Figure 37: The plot of T_c vs. ρ_0 for $x = 0.22$, where ρ_0 is a fitting parameter in $\rho_{ab} = \rho_0 + \beta T^n$. The open triangles denote the data in the orthorhombic phase and the closed ones denote the data in the tetragonal phase of LSCO. With increasing pressure, ρ_0 increases and T_c decreases. Ambient pressure values of ρ_0 are also plotted for $x = 0.26$ by an asterisk. The extrapolated value of ρ_0 at $T_c = 0$ for $x = 0.18$ and 0.22 is higher than for $x = 0.26$.

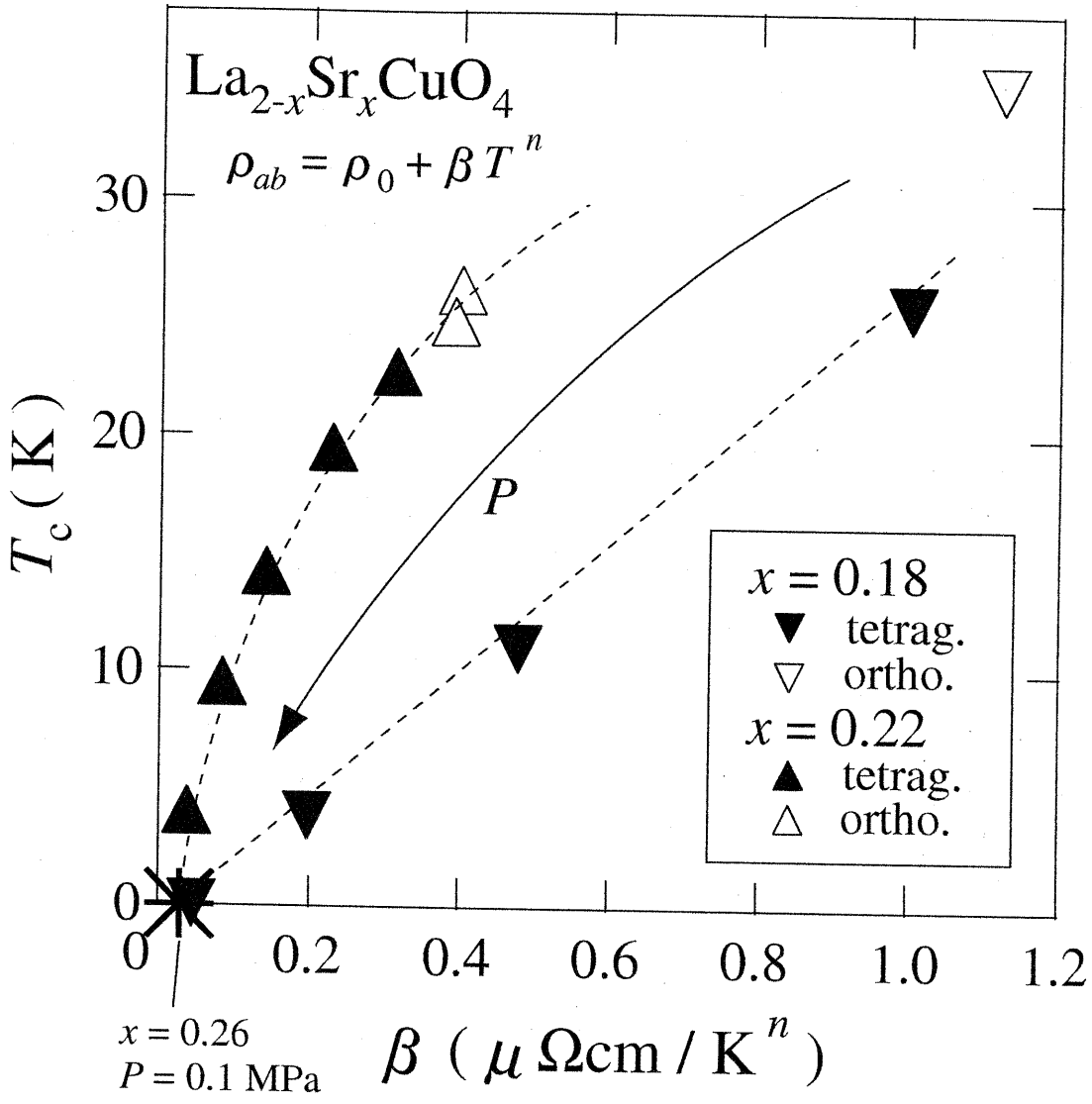

Figure 38: The T_c-β plots for $x = 0.18$, 0.22, and 0.26, where n is a fitting parameter in $\rho_{ab} = \rho_0 + \beta T^n$. The open triangles are the data in the orthorhombic phase and closed ones are the data in the tetragonal phase for $x = 0.18$ and 0.22. The asterisk is the data for $x = 0.26$ at ambient pressure. With increasing pressure n increases for $x = 0.18$ and 0.22. The extrapolated values of n to $T_c = 0$ for $x = 0.18$ and 0.22 agree well with the values for $x = 0.26$

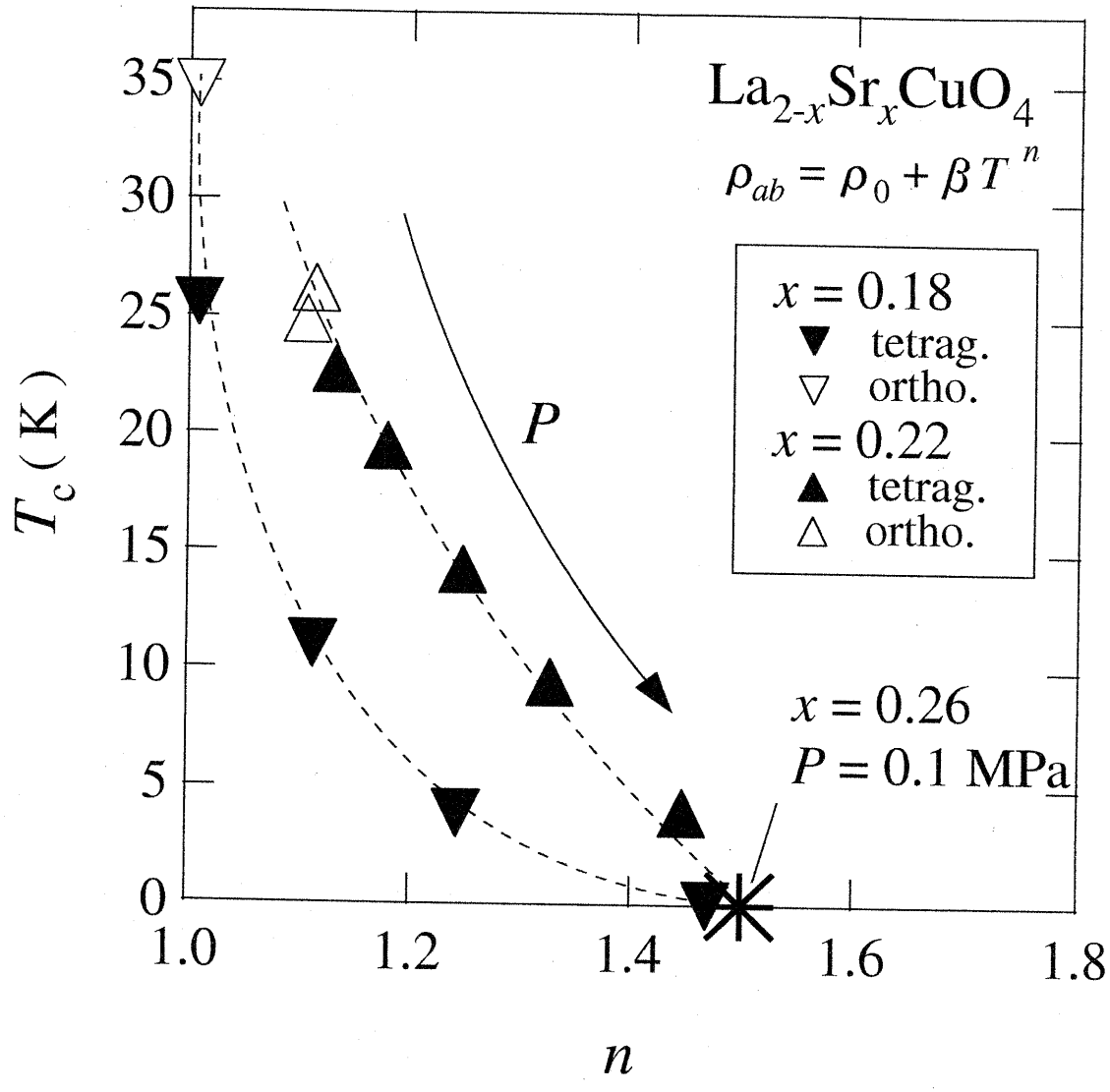

Figure 39: The T_c-n plot for $x = 0.18$, 0.22, and 0.26, where n is a fitting parameter in $\rho_{ab} = \rho_0 + \beta T^n$. The open triangles are the data in the orthorhombic phase and closed ones are the data in the tetragonal phase for $x = 0.18$ and 0.22. The asterisk is the data for $x = 0.26$ at ambient pressure. With increasing pressure β decreased for $x = 0.18$ and 0.22. The extrapolated values of β to $T_c = 0$ for $x = 0.18$ and 0.22 agree well with the values for $x = 0.26$

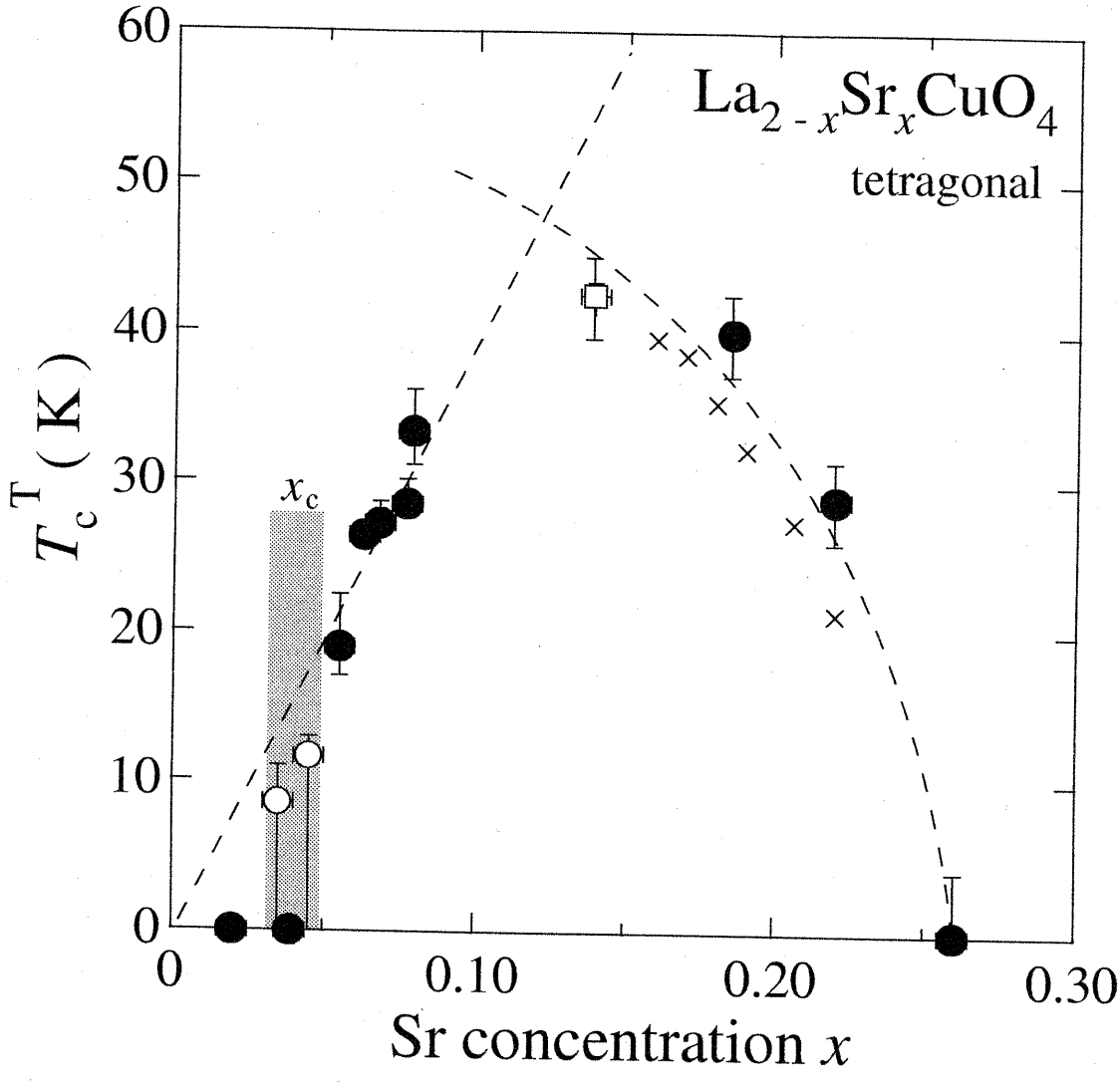

Figure 40: The phase diagrams of the T_c^T which is the T_c in the tetragonal phase at ambient pressure. The crosses and open box are T_c^T estimated from the reported data of polycrystals[6] and single crystals.[8] T_c^T is proportional to x over $x \sim 0.05$ and change discontinuously around $x_c \sim 0.05$. The open circles are T_c^T estimated from the extrapolation of T_c' in the Fig.26 and 28 which are not bulk superconductivity. The broken line is guide for the eyes.

公 表 論 文

Correlation between superconductivity and in-plane resistivity in $La_{2-x}Sr_xCuO_4$

J. Hori, S. Iwata, H. Kurisaki, F. Nakamura, T. Suzuki, and T. Fujita

Journal of the Physical Society of Japan,**71**(2002)1346–1352.

参考論文

(1) **Superconductor–insulator transition in under–doped cuprates**
T. Fujita, J. Hori, S. Iwata, Y. Yoshino, H. Kurisaki, T. Goko, Y. Yamane, and F. Nakamura
Physica C **364–365** (2001) 274–277.

(2) **Effect of orthorhombic distortion on superconductivity in $La_{2-x}Sr_xCuO_4$**
T. Goko, F. Nakamura, J. Hori, and T. Fujita
Physica B **284–288** (2000)1053–1054.

(3) **Superconductivity in the tetragonal lattice of underdopd $La_{2-x}Sr_xCuO_4$**
T. Fujita, J. Hori, T. Goko, N. Kikugawa, and S. Iwata
Physica C **341–348** (2000)1939–1940.

(4) **Enhancement of conduction along the *c* axis in $La_{2-x}Sr_xCuO_{4-\delta}$ due to the impurity scattering**
N. Kikugawa, J. Hori, F. Nakamura, and T. Fujita
Journal of the Physical Society of Japan, **69** (2000) 1177–1180.

(5) **Role of two–dimensional electronic state in superconductivity in $La_{2-x}Sr_xCuO_4$**
F. Nakamura, T. Goko, J. Hori, Y. Uno, N. Kikugawa, and T. Fujita
Physical Review B **61** (2000)107–110.

(6) **T_c enhancement in $La_{2-x}Sr_xCuO_4$ by anisotropic pressure**
T. Fujita, J. Hori, T. Goko, and F. Nakamura
International Journal of Modern Physics B **13** (1999) 3655–3659.

(7) **T_c enhancement in $La_{2-x}Sr_xCuO_4$ under anisotropic pressure**
F. Nakamura, J. Hori, T. Goko, Y. Uno, N. Kikugawa, and T. Fujita
Journal of Low Temperature Physics, **117** (1999)1145–1149.

(8) **Impurity scattering effect on the anisotropic resistivity for $La_{2-x}Sr_xCuO_{4-\delta}$ with a wide range of *x***
N. Kikugawa, J. Hori , F. Nakamura, and T. Fujita
Journal of Low Temperature Physics, **117** (1999)1139–1143.

(9) **Transport properties of $La_{2-x}Sr_xCuO_4$ under pressure**
F. Nakamura, T. Goko, J. Hori, Y. Uno, N. Kikugawa, and T. Fujita
Physica C **317–318** (1999)366–372.